Carbon Export and Fate Beneath a Dynamic Upwelled Filament off the California Coast

Hannah L. Bourne[1], James K. B. Bishop[1,2], Elizabeth J. Connors[1,3], Todd J. Wood[2]

[1]Dept. of Earth and Planetary Science, University of California, Berkeley, CA, 94720, USA
[2]Earth and Environmental Sciences Division, Lawrence Berkeley National Laboratory, Berkeley, CA, 94720, USA
[3]Scripps Institution of Oceanography, La Jolla, CA, 92093, USA

Correspondence to: James K.B. Bishop (jkbishop@berkeley.edu)

Abstract. To understand the vertical variations of carbon fluxes in biologically productive waters, four autonomous Carbon Flux Explorers (CFEs), ship-lowered CTD-interfaced particle sensitive transmissometer and scattering sensors, and surface drogued sediment traps were deployed in a filament of offshore flowing, recently upwelled water, during the June 2017 California Current Ecosystem – Long Term Ecological Research process study. The Lagrangian CFEs operating at depths from 100-500 m yielded carbon flux and its partitioning with size from 30 µm –1 cm at three intensive study locations within the filament and in waters outside the filament. Size analysis codes intended to enable long-term CFE operations independent of ships are described. Different particle classes (anchovy pellets, copepod pellets and >1000 µm aggregates) dominated the 100-150 m fluxes during successive stages of the filament evolution as it progressed offshore. Fluxes were very high at all locations in the filament; below 150 m, flux was invariant or increased with depth at the two locations closer to the coast. Martin curve 'b' factors (± denotes 95% confidence intervals) for total particulate carbon flux were +0.37±0.59, +0.85±0.31, -0.24±0.68, and -0.45±0.70 at the three successively occupied locations within the plume, and in transitional waters, respectively. Interestingly, the flux profiles for all particles <400 µm were a much closer fit to the canonical Martin profile (b -0.86); however, most (typically >90 %) of particle flux was carried by >1000 µm sized aggregates which increased with depth. Mechanisms to explain the factor of three flux increase between 150 and 500 m at the mid plume location are investigated.

1 Introduction

Carbon export driven by the biological carbon pump, the process by which photosynthetically derived biomass is transported out of the surface layer, is an important component of the global carbon cycle. Atmospheric carbon concentrations are in part controlled by the depth at which sinking organic matter is remineralized (Kwon et al., 2009) yet the fate of carbon exported to deeper waters beneath highly productive coastal regions is poorly understood. Current estimates for global carbon export range from 5 to >12 Pg C yr^{-1} (Boyd and Trull, 2007; Henson et al., 2011; Li and Cassar, 2016; Dunne et al., 2005; Siegel et al., 2014, 2016; Yao and Schlitzer, 2013). Because coastal upwelling regions are such productive and unique ecosystems with

complex current interactions, a question to be asked is: "Is export of material to depth in these systems different than in open ocean environments?". If so, knowing the rules governing particulate carbon export and remineralization in these regions will significantly advance carbon cycle simulations of CO_2 uptake by the oceans.

35   While ocean colour satellites provide temporal and spatial scale of phytoplankton biomass when clouds permit, flux beneath the euphotic zone is much more difficult to observe and therefore not as well known. A number of recent studies have noted discrepancies in reconciling meso- and bathypelagic activity with current euphotic zone flux estimates (Banse, 2013; Burd et al., 2010; Ebersbach et al., 2011; Passow, 2012; Stanley et al., 2012). Measurements of new production (NP, Eppley and Peterson, 1979) should balance particle export measured at the same time if gravitational particle sinking dominates export;

40   however, NP often is higher than particle export (Bacon et al., 1996; Estapa et al., 2015; Stukel et al., 2015). Mechanistic understanding of these differences is thus important to food web models.

The strength and efficiency of the biological carbon pump is governed by complex interactions between phytoplankton, zooplankton and physical mixing. The Martin Curve (Equation 1), an empirical relationship, was derived from surface tethered sediment trap observations made in the north Pacific during the VERTEX program (Martin et al., 1987),

$$F = F_{\text{ref}} \left(\frac{z}{z_{ref}} \right)^{b} \qquad (1)$$

where F is flux at depth z; F_{ref} is the flux measured at a reference depth z_{ref} (usually near the base of the euphotic zone) and b is a constant. Martin et al. (1987) found best fits with b = -0.86; The choice of z_{ref} does not influence the derived the b value.

50   Bishop (1989) compared the Martin and six other formulations for particle flux at depth in the open ocean and found that the Martin Curve for predicting flux was most robust; while many profiles were fit with the classic Martin "b" factor of -0.86, the study found (in rare cases) b values of -0.3 to -1.5. Subsequent studies in the open ocean have yielded similarly varying b values, and all show the expected flux decrease with depth (Fig. 1) (Buesseler et al., 2007; Lutz et al., 2007; Marsay et al., 2015).

55   If all material sinking to depth is assumed to be gravitationally exported material originating from a stable photosynthetically derived source in the euphotic zone, an increase of material with depth should not occur. However, flux profiles that do not decrease monotonically with depth as predicted by Martin's formula have been observed, especially in regions that are both physically and biologically dynamic (e.g., Bishop et al., 2016 in the Santa Cruz Basin; Giering et al., 2017 in the North Atlantic), suggesting additional mechanisms contributing to particle flux are at play.

60   The California Current, the eastern boundary current of the North Pacific gyre, flows south from the sub-arctic North Pacific. Beneath it, the subsurface California Undercurrent flows poleward at depths between 200 and 500 m, with strong seasonal

variability (Lynn and Simpson, 1987). Along the coast, the complex interactions of filaments, geostrophic flow, wind-driven Ekman transport and mesoscale eddies distribute coastal waters. This leads to a heterogeneous pattern of productivity in surface waters with some regions (often in the vicinity of headlands) having very high productivity near centres of coastal upwelling, while others have intermediate productivity spurred by wind stress curl upwelling, and other low productivity regimes which reflect the onshore flow of oligotrophic waters (Gruber et al., 2011; Ohman et al., 2013; Siegelman-Charbit et al., 2018). In the summer, winds blowing south along the California coast cause surface waters to divert to the west, which allows deep nutrient rich cold water to come to the surface. This water coming to the surface moves offshore in filaments which can extend offshore several hundred kilometres.

The California Current Ecosystem Long-Term Ecological Research (CCE-LTER) process study (June 1 - July 2, 2017; P1706) gave us the opportunity to observe carbon flux profiles beneath a rapidly evolving surface filament over its lifetime, and to understand the magnitude, scales, and mechanisms of coastal production and its transport. During the study, we deployed Carbon Flux Explorers (CFE; Bishop et al., 2016, and Bourne et al., 2019) to depths of 500 m to observe particle flux variability, and specifics of particle classes contributing to flux. Figure 2 shows the locations of CFE deployments and other activities during the CCE-LTER study, the Santa Cruz Basin (SCB) study site of Bishop et al., (2016), as well as the coastal station VERTEX 1 (Martin et al., 1987). The CCE-LTER study combined spatial surveys, three cross-filament CTD transects, and four sequentially numbered multi-day quasi-Lagrangian intensive sampling "cycles" within and outside of the filament. Cycles 1 to 4 correspond to locations 1 to 4 which are referred to as L1 to L4 below. L1, L2 and L4 represent sampling during the early, intermediate, and late stages of filament evolution. The order of occupations of L3 (outside of the filament) and L4, enabled a more complete view of filament evolution.

In this study, we report autonomously measured carbon flux profiles in the mesopelagic zone beneath a filament of upwelled water off the coast of California and the finding at two locations (L1 and L2) that flux was invariant or increasing with depth, while flux decreased more slowly than predicted by the Martin formula at two other locations. We explore mechanisms for these flux profile observations. In the following discussion, we use the term "non-classic" to represent strong departures from the classic (b = -0.86) Martin curve.

1.1 Study Area

The June 2017 CCE-LTER process study aboard R/V Revelle followed a strong filament of upwelled cold, high-salinity westward-flowing water off the coast of California. In late May, cold water upwelled along the coast due to the intensification of upwelling favourable north to south winds; shortly thereafter a filament developed near Morro Bay (35° 22' N, 122° 52' W, Fig. 2) and began propagating westward (Figs. 3a, b). Eventually, the filament extended 250 km offshore (Figs. 3c, d). By mid-June, the western most filament waters began to slow and developed into a cyclonic eddy which became pronounced in maps of sea surface height by the end of June (Fig. 4); locations L1–L4 are depicted in the maps.

2. Methods

2.1 Remote Sensing Data

Satellite retrievals of sea surface temperature (SST), sea surface chlorophyll, and euphotic zone depth at 4 km spatial resolution, and averaged at 1-day or 8-day temporal resolution from SMPP VIIRS (Visible Infrared Imaging Radiometer Suite) and
100 MODIS Aqua spacecraft were obtained from the NASA ocean colour archive (https://oceancolor.gsfc.nasa.gov/l3/). We similarly obtained Coastal Zone Colour Scanner (CZCS) data to provide context for the June 1984 Martin et al. (1987) VERTEX 1 station. Sea surface height (SSH) data (derived from as suite of spacecraft) were downloaded from the NASA Jet Propulsion Laboratory at a 1/6th degree and 5-day resolution (https://podaac.jpl.nasa.gov/; doi: 10.5067/SLREF-CDRV1). Imagery was used in Figures 3 and 4 to provide large scale context for the study. Daily imagery was used to provide location
105 scale views of CFE, drifter, and sediment trap deployments, and CTD casts. Fig. 5 depicts the spatial context for observations at L2; contexts for L1, L3, and L4 during successive stages of filament evolution are in Appendix figures A1-1, A1-2, A1-3.

2.2 Carbon Flux Explorer (CFE)

The CFE and the operation of its particle flux sensing Optical Sedimentation Recorder (OSR) have been discussed in detail in Bishop et al. (2016). Briefly, once deployed, the CFE dives below the surface to obtain observations at target depths as it drifts
110 with currents. The OSR wakes once the CFE has reached the target depth. On first wake-up on a given CFE dive, the sample stage is flushed with water and images of the particle-free stage are obtained. Over time, particles settle through a 1-cm opening hexagonal celled light baffle into a high-aspect ratio (75° slope) funnel assembly before landing on a 2.54 cm diameter glass sample stage. At 25-minute intervals, particles are imaged at 13 μm resolution in three lighting modes: dark field, transmitted and transmitted-cross polarized. Particles build up sequentially during the imaging cycle over 1.8 hours, at which time another
115 cleaning occurs and a new reference image set is obtained; the process repeats. After ~6 h at a target depth, the OSR performs a final image set, cleaning cycle and reference image set, and the CFE surfaces to report GPS position, CTD profile data and OSR engineering data, and then dives again.

Four CFEs were deployed pair wise at each of the four locations (Figs. 2 and 3; Table 1). Two CFEs, referred to here as CFE-Cals (CFE-2 and CFE-4), were built to collect calibration samples as described in Bourne et al. (2019). These new CFEs were
120 built with SOLO-II floats, with a threefold greater buoyancy adjustment capability than the older CFEs (CFE-1, and CFE-3) which could not carry the samplers. CFE-Cals were programmed to drift at 150 m and were typically deployed twice for 20-hours at each location. We found that the concave bladder housing of the SOLO-II float trapped air in a way that made it more difficult for the CFE-Cals to attain a stable target depth. This was a particular problem when the CFEs were launched in calm conditions. We found that copious seawater rinsing of the CFE-Cal SOLO II bladder assembly prior to launch and ensuring
125 that the CFE-Cals were horizontal when released solved this problem. The two other CFEs, CFE-1 and CFE-3, were programmed to drift at three depths (CFE-1 and 3 are referred to as profiling CFEs) and did not have depth stability issues. At

L1, bottom depth was ~450 m and we limited CFE dives to shallower than 300 m. At offshore locations L2, L3 and L4 the three target depths were 150, 250 and 500 m. The profiling CFEs (CFE-1 and CFE-3) were deployed at each location for 3 to 4 days. At L3, CFE-3 was attacked twice violently by a large (length greater than the 2.3 m height of the CFE with antennas) short-fin Mako shark as we watched. The first high velocity charge hit the OSR directly and had no effect on the CFE; the second charge hit the SOLO top cap and antenna assembly and broke the float causing CFE-3 to sink in seconds. Consequently, only CFE-1 made flux observations deeper than 150 m at L3 and L4. We deployed CFEs 24 times; 21 yielded results reported here (Table 1); two early deployments of CFE-Cals were not useful, and imagery from CFE-3 at L3 was lost due to the shark attack.

2.2.1 Reduction of OSR Transmitted Light Images

Transmitted light colour images were normalized by an in-situ composite image of the clean sample stage following Bishop et al. (2016) yielding a map of fractional transmission corrected for inhomogeneities of the light source. Attenuance (ATN) values were then calculated by taking the $-\log_{10}$ of the normalized image using the green colour plane. Pixels with an attenuance value less than 0.02 attenuance were defined to be background. Pixels above the threshold were integrated across the sample stage then divided by total number of pixels in the sample stage area to yield attenuance (ATN). Figure 5 depicts time series of attenuance (in mATN units) at different depths for the mid-filament location L2; similar data from L1, L3, and L4 are in Appendix Figs. A1-1, A1-2 and A1-3, respectively. The sawtooth attenuance trends in Fig. 5 reflect progressive particle accumulation on the imaging stage followed by stage cleaning which brings attenuance back down to baseline. Multiplying attenuance by the sample stage area (5.07 cm^2) gives sample Volume Attenuance (VA, units: mATN-cm^2, Bourne et al., 2019). VA can be thought of as the optical volume of particles on the sample stage. In this paper we focus on light attenuation (derived from transmitted light images) as proxy of carbon flux because the proxy has been calibrated (Bourne et al., 2019).

2.2.2 Conversion of Volume Attenuance to POC flux.

Volume Attenuance (VA) has been calibrated in terms of particulate organic carbon and nitrogen (POC and PN) loading (Bourne et al., 2019). VA is converted to Volume Attenuance Flux (VAF) by normalizing VA by deployment time and scaling by the area of the funnel opening. The regression for measured POC flux (mmol C m^{-2} d^{-1}) against VAF (units mATN-cm^2 cm^{-2} d^{-1}) is given by Equation 2 (Bourne et al., 2019).

$$POC\ flux = 0.965\pm0.093*VAF - 1.1\pm1.5\ mmol\ C\ m^{-2}\ d^{-1} \tag{2}$$

VAF is ~4 times more precisely determined than POC flux (Bourne et al., 2019) and thus we use it as the X-axis variable. The regression R^2=0.897 and the ± values denote one standard deviation of slope and intercept, respectively. For simplicity, we use a conversion factor of 1.0 to scale VAF to POC flux. The intercept is not significantly different from zero and is ignored. The CFE derived optical proxy for POC flux is referred to as POC$_{ATN}$ flux below.

2.2.3 Particle Size Distributions

Three methods were used to determine particle size distributions in CFE imagery: (1) A computationally efficient code that measures particle area and attenuation (Bourne, 2018), (2) manual identification and counting of particle classes, and (3) a hybrid of image analysis and visual verification of identified particles.

Transmitted light images from the CFEs were processed to attenuance units following Bishop et al. (2016). Results were saved as imagery in attenuance units where counts in each 8-bit (red, green, blue) colour plane are scaled so that 100 counts = 1 attenuance unit. The complete set of 1600 CFE transmitted light images and corresponding attenuance images are available through the Biological and Chemical Oceanography Data Management Office (BCO-DMO) at the Woods Hole Oceanographic Institution (Bishop, 2020a).

For size analysis, the RGB image is converted to an 8-bit grayscale image. The 5 Mpixel SUMIX imager used in the CFE employs a Bayer filter that allocates in a checkerboard pattern 50% of the pixels to green and 25% to each of the blue and red colour channels. In the case of transmitted light imagery, we have found little difference in attenuance values from the three colour planes (Bourne et al. 2019); however, this is not true of imagery in dark field illumination. We choose to set the definition of a "particle" as having 4 contiguous pixels above threshold in order to provide compatibility with interpretation of darkfield imagery, where colour is important. A 4-pixel particle is having an area of 676 μm^2 or an equivalent circular diameter (ECD) of 29 μm.

Method 1. Threshold variation.

Bourne (2018) developed a computationally efficient nearest-neighbour particle detection algorithm to measure attenuance size-distributions in CFE images. This was an important first step towards fully autonomous observations as this scheme can run aboard the CFE. Unlike the 'stage' integration (Sect. 2.2.1), particle size analysis requires a choice of an attenuance count threshold to distinguish particles and differentiate them from background. Choosing too low of a threshold can increase the false detection of particles due to imperfections of lighting and sensor noise. Bourne (2018) studied thresholds from 0.02 to 0.20 attenuance units. Even at the highest threshold setting, the method failed to separate touching 250 μm ECD ovoid faecal pellets (Fig. 6) which constituted a significant component of particle flux at 150 m at L2. In this method, as well as Method 3 (below), particle size distributions were determined in the last image of a cycle before the imaging stage was cleaned. If overlapping particles were present, the previous image in the series would be used instead. This choice was made manually but could be automated. Bourne (2018) used a threshold attenuance of 0.12 to systematically analyse 143 image cycles using this method.

Method 2. Manual Counting

CFE images from L2 were manually enumerated for ovoid faecal pellets and >1000 μm sized aggregates using a combination of transmitted light and darkfield imagery (Connors et al., 2018; Bourne et al. 2019).

Method 3. ImageJ size analysis and secondary processing

195 In Method 3, the software package ImageJ 1.52 (IJ, National Institutes of Health) was used for particle size analysis. The advantage of ImageJ is that the analysis provides a rich statistical description of the individual particles that can be used aid in particle class analysis. In this method, we manually inspected the 4 to 5 sequential attenuance images taken during each image cycle to determine the point of onset of particle overlap. The attenuance image was subtracted from the preceding attenuance image of the clean sample stage. A threshold of 4 counts (0.04 ATN) and above was used to define the presence of particles

200 (2 counts higher than used for calculation of VA). At this threshold setting, large aggregates were fully detected; however, touching particles – particularly 200-400 μm sized faecal pellets (Fig. 6) were not separable. Each IJ-identified "particle" with multiple identical units was counted and these counts assigned to its sequence number. Inspection of the imagery also identified touching large aggregates which were similarly treated. During secondary data processing, the area of each multi-unit "particle" was divided by the number of subunits, and its particle number was changed from 1 to the determined count.

205 Examples of touching ovoid particles are found in Figure 6. Living organisms rarely appeared in images; when they did appear, we were able to identify pteropods, amphipods, copepods, siphonophores, acantharia, radiolaria, and foraminifera. These "living" particles were removed from the secondary processed data. Total particle attenuance (average particle attenuance times particle area) and particle number were binned into 65 logarithmically spaced size categories from (30 μm to 20000 μm). A total of 267 image pairs were analysed; these combined flux results for each of 89 CFE dives are available online through

210 the Biological and Chemical Oceanography Data Management Office (BCO-DMO; Bishop, 2020b). Float CTD results are similarly archived (Bishop, 2020c).

Data from each image cycle were weighted by the total number of images in that cycle; data from the multiple imaging/cleaning cycles during a dive were binned and weighted by the duration of each imaging cycle. The particle attenuance and number size-binned data were scaled to convert results to flux units (mATN–cm^2 cm^{-2} d^{-1}; and number m^{-2} d^{-1}). The partitioning of

215 particle flux by size was simplified to five size categories: 30-100, 100-200, 200-400, 400-1000, and >1000 μm. In the process, ATN and number fluxes at category boundaries were determined by interpolation of the detailed cumulative flux – size distributions. The 200-400 μm bin primarily was populated by the numerous ovoid pellets. The >1000 μm bin was dominated by aggregates.

Figure 7 displays normalized cumulative size distributions prior to and after secondary processing for all CFE dives at L2. The

220 point of this labour-intensive computer-aided approach was to provide a basis for future code development. The scientific outcome of this analysis is a description of the number and attenuance fluxes of different sized particles and how these fluxes change down the water column during the CCE-LTER process study.

Method intercomparison. Figure A1-4 in Appendix A compares normalized-cumulative-attenuance flux and normalized-cumulative-number flux size-distributions from Methods 1 and 3 at locations (L1–L4). Some differences are attributed to

225 independent choices of which image sets to analyse (137 vs. 267) using the two methods; never-the-less, we found good

agreement between the methods for data from 250 m and deeper. The poorer agreement in size distributions from 150 m is due to the high threshold (0.12 attenuation) of Method 1 failing to detect large aggregates as whole particles and also the problem of touching faecal pellets, which dominated samples at 150 m at L2 (Fig. 6).

Figure 8 compares profiles of aggregate (>1000 µm) and pellet (200-400 µm) number fluxes with manually determined counts of these classes at location L2. Although the data were calculated in slightly different ways, Method 3 aggregate flux and manually determined aggregate flux closely matched. The Method 3 pellet flux agreed closely with manual counts at 150 m, but overestimated results at 500 m by a factor of 5. To understand this difference, we graphed particle attenuation for all 150–400 µm sized particles at 150 m at L2. Results showed a cluster of particles >200 µm in size with attenuation values >0.25 which suggested that the cluster was due to ovoid faecal pellets. We calculated the ratio of the number of particles >0.25 attenuation to total particles and used the ratio to correct the Method 3 counts. Results brought the Method 2 and Method 3 counts at L2 into agreement (Appendix A, Table 1-1). We applied this approach to L1, L3 and L4 data (Fig. 8). L4, in particular, showed high numbers of particles in the 200-400 µm category which originated from the fragmentation of large low attenuation aggregates; only 15% of particles had attenuation above 0.25 at 250 and 500m.

2.2.4 Sources of uncertainty of POC$_{ATN}$ flux

Calibration studies by Bourne et al. (2019) were restricted to depths near 150 m due to logistical reasons including ship time, the need for replication of results, and for comparison of POC$_{ATN}$ fluxes with data from surface drogued sediment traps (Sect. 2.4 below) which were restricted to the upper 150 m. We do not believe that this is a major limitation because samples collected at 150 m covered a wide range of size distribution and particle types that were also found deeper in the water column. Furthermore, large particles sampled by large volume *in-situ* filtration show little shift in organic carbon percentages from the base of the euphotic zone to 500 m (e.g., Bishop et al., 1986). For these reasons, we assume that the uncertainty of our present calibration is ~9% (±1 S.D.; Eqn. 2). More calibration sampling is desired.

During review, we were asked to estimate the contribution of counting statistics to the uncertainty of POC$_{ATN}$ flux for the >1000 µm particle class vs. that for smaller size classes. As we show below that the large aggregate size fraction dominates total POC$_{ATN}$ flux, it is also true that this flux is determined by a relatively few numbers of aggregates arriving during each image cycle. We assume Poisson counting statistics, where the relative standard deviation (RSD) counting error for n particles is $\sqrt{n}/n$, and that the RSD can be applied to both number flux and attenuance flux. Figure A1-5a shows representation of this error for the 200-400 µm and for >1000 µm categories; two cases are calculated: that for individual dive results and for the grand average of all dives at 4 depth horizons at each location. Count-related errors for individual dives for the 200400 µm and >1000 µm categories were typically <10% and <30%, respectively; similarly, for pooled dive results such errors were typically <5% and 20%. At L3 where fluxes were low, count related errors for POC$_{ATN}$ flux in 200-400 µm and for >1000 µm categories were typically 20% and 40%, respectively; pooled results gave ~15% and 30% errors. Figure A1-5b illustrates the

combined effect of counting error and 9% calibration uncertainty for individual dives at L2 and L3 (as plotted in Fig 15a below). These errors are minor compared to the range of POC_{ATN} flux values observed. The complete dive averaged data sets with error estimates are available as supplemental on-line material. Note: n values used for error calculation listed in the supplemental data set are not integers due to number fluxes being based on extrapolations to the boundaries of the 5 size categories.

We assume for the following discussion that the VAF:POC flux relationship has a 9% uncertainty and is invariant with depth; furthermore, errors due to the statistical frequency of particles in different size categories is also deemed a minor influence on our interpretations.

2.3 Acoustic Doppler Current Profiler (ADCP) and other CTD data

Current velocity in u (east positive) and v (north positive) components from the hull mounted RD Instruments 150 kHz narrow band Acoustic Doppler Current Profiler (ADCP) were averaged over 30-minute intervals during the times of CFE deployment. The 150 kHz data were limited to the upper 400 m. CFE drift velocities were calculated based on CFE dive locations and times. Combined ADCP and CFE drift results are shown in Figure 9.

The hydrographic context for our study was provided by CTD profiles of T, S, potential density anomaly (σ_θ), photosynthetically active radiation (PAR), chlorophyll fluorescence (Seapoint Inc.), turbidity at 810 nm (Seapoint Inc.) and transmission at 650 nm (WETLabs, Inc. Philomath, OR). Particle optics were kept clean as detailed in Bishop and Wood (2008). The CTD/Rosette casts were usually made in close proximity to a surface drogued productivity array which served as the Lagrangian reference for studies at each location. Nutrient data from the CTD/Rosette samples used in this paper are archived in the CCE-LTER data repository (https://oceaninformatics.ucsd.edu/datazoo/catalogs/ccelter/datasets).

Transmissometer derived beam attenuation coefficient (m^{-1}) multiplied by a factor of 27 is used to calculate particulate organic carbon (POC) concentration (μM; Bishop and Wood, 2008). The Seapoint fluorescence data were offset by subtraction 0.05 units and residual values lower than 0.02 were determined to be below detection. The CTD/Rosette also carried an Underwater Vision Profiler particle imaging system (UVP5-hd; Hydrooptic, France) capable of resolving particles >64 μm in reflected light. Data are archived at https://ecotaxa.obs-vlfr.fr/part/ under the Project: UVP5hd CCELTER 2017. We used the "non-living" particle concentrations averaged over 5 m which were representative of particles present in ~180 L. We pooled and further depth-averaged all CTD cast data at each location to achieve an equivalent water volume of ~2000 L to improve the statistics of the number concentrations of >1000 μm aggregates. In this paper we focus on the >1000 μm fraction, although all size fractions have been treated identically. Further detailed analyses of UVP5 imagery are beyond the scope to the paper.

2.4 New Production based Carbon Export (POC$_{NP}$ flux) and Particle Interceptor Trap flux

Euphotic zone new production (NP) measurements at locations L1, L2, L3 and L4 (converted to carbon units) were 189 ± 21, 156 ± 77, 63 ± 33, and 19 ± 3 mmol C m^{-2} d^{-1}, respectively (Kranz et al., 2020). We refer to these data as POC$_{NP}$ flux. POC fluxes from deployments of surface drogued PIT traps deployed to 150 m are from Stukel and Landry (2020). These values are referred to as POC$_{PIT}$ flux.

In this study, CFEs were programmed to dive deeper than 100 m and POC$_{ATN}$ fluxes were lower than POC$_{NP}$ values at all locations except at L4, the last occupation of the filament; in this case POC$_{ATN}$ flux exceeded POC$_{NP}$ by a factor of >2 at 250 m suggesting a recent decline in carbon export. Nitrate and beam attenuation coefficient (POC) changes (Table 2) allow an estimate POC$_{NP}$ flux for the 9-day interval spanning the occupations of L2 and L4. We have confidence in this calculation since a sediment trap array, deployed late in the study at L2b tracked the water to L4 (Kranz et al., 2020); furthermore, L2b and L4 salinity profiles were virtually identical (Fig. 10) confirming that the surface water masses encountered at L2 were nearly the same as at L4. Following Johnson et al. (2017), we subtract 0–45 m stocks of dissolved nitrate at L2b from L4 (Table 2) and multiply this change by the molar ratio of photic layer plankton C/N. Johnson et al. (2017) used a C/N ratio of 6.6; we used a C/N of 6.4 (Stukel et al., 2013). We chose 45 m as the integration depth as dissolved nitrate profiles at the two sites converged at this depth (Fig. 10) and also because 45 m was close to the euphotic zone depth at L4. The calculation yielded an averaged POC$_{NP}$ flux = 111.3 ± 32.2 (S.D.) mmol C m^{-2} d^{-1} over 9 days, similar to measured POC$_{NP}$ at L2, but a factor of 6 higher than reported at L4 by Kranz et al. (2020). POC inventory changes (Table 2) from L2b to L4 between the two times implied an average POC loss rate of 33 mmol C m^{-2} d^{-1}. Crustacean grazers have assimilation efficiencies of 70%, with the remaining fraction voided as faecal pellets. Export from this POC loss would add ~10 mmol C m^{-2} d^{-1}. Averaged export from L2b to L4 sums to ~120 mmol C m^{-2} d^{-1}.

3. Results

3.1 Spatial Context and Water column environment

CFE deployment locations and times are summarized in Table 1 (above). Table 2 summarizes mixed layer and euphotic zone properties for each intensive study location. Figures A1-1(b), 5 (above), A1-2(b), A1-3(b) show satellite retrieved surface chlorophyll fields from SMPP-VIIRS with superimposed locations of CFE surfacing and CTD/optics profiles, and tracks of the surface drogued particle interceptor trap (PIT) array, and of the drogued productivity (PROD) array at locations L1 – L4, respectively. At locations L1 and L4, the Lagrangian CFEs tracked well with all deployed systems; at L2, there was a divergent behaviour of CFEs, PIT and drifters with CFE and PIT array remaining closest; at L3, the CFE and PIT arrays maintained a similar track. At all locations, CFE trajectories closely matched ADCP velocities (Fig. 9) and the patterns of flow suggested by sea surface altimetry (Fig. 4).

Figure 11 shows time series depth-plots of T, S, potential density (σ_θ), chlorophyll fluorescence, transmissometer-derived POC and turbidity. POC and Salinity – potential density transects are shown in Figure 12 along with POC / Salinity – potential density time series at the 4 locations. We reordered the time axis in these figures to make data from in-filament locations L1, L2, and L4 more logically related and separate from the out-of-filament transitional waters at L3. L2 is split temporally into L2a and L2b for reasons outlined below.

3.1.1 Location 1

Study site L1 was located in the middle of a 50 km wide 500 m deep trough (Fig. 2) approximately 25 km offshore of Morro Bay, CA. The SMPP-VIIRS chlorophyll (Fig. A-1(b)) shows that early CFE and CFE-Cal deployments took place in close proximity to very high chlorophyll waters. Upwelling was active as evidenced by cold, high-salinity surface waters and low stratification (Fig. 10, 12). The 24-hr mixed layer depth (MLD_{24}), defined by a potential density increase of 0.05 kg m^{-3} relative to surface values (Bishop and Wood, 2009), averaged 19 m (range from 13 to 25 m) and matched euphotic zone depth (16$\pm$4 m) (Table 2). Mixed-layer nitrate dropped from 10.2 to 5.4 μM over several days. CFE Attenuance time-series showed an early high flux event (Fig A1-1(a)). ADCP derived currents (Fig. 9a) show strong tidal fluctuation; however, there was a net southwest transport of water in the upper 50 m at a velocity of 0.06 m s^{-1}, at 0.02 m s^{-1} between 100 and 200 m, and at 0.04 m s^{-1} between 200 and 300 m. Deployed instrument trajectories were consistent with ADCP results.

3.1.2. Location 2

Site L2, was located 110 km offshore. MLD_{24} averaged 26 m and matched the euphotic zone depth of 25 $\pm$ 3 m. The base euphotic zone was bounded by the σ_θ = 25.5 kg m^{-3} isopycnal. The temperature and salinity profiles from CFE-1 and CFE-3 (Bishop, 2020c) were in close agreement with CTD casts 25-30 (locations Fig 5(b)), whereas the subsequent CTD cast data and L2 diverge. The early CTD casts revealed a stronger halocline and pycnocline, with saltier, denser waters between about 25 and 150 m, indicating upwelling in this part of the timeseries (Fig. 10 and 11). We thus treat the first 6 CTD casts as representative of CFE deployment 2a, and subsequent casts as 2b. Averaged 0-20 m nitrate in was 8.6 and 7.8 μM during 2a and 2b, respectively; salinity values were identical. Chlorophyll fluorescence and transmissometer derived POC decreased by a factor of two during observations at 2a and 2b (Figs. 11(d) and 12(a)). During the later stages CFE observations, SMPP-VIIRS surface chlorophyll fields were almost uniform (1.8 to 2.5 mg Chl-a m^{-3}; Fig. 5(b)).

CFE-1 and CFE-3 were launched in a fast-moving part of the filament and transported to the WNW (Fig. 5(b)) and separated from surface drogued PIT array and productivity drifter; twenty hours later, CFE-Cals 2 and 4 similarly tracked to the WNW on a parallel course to CFEs 1 and 3 (Fig. 5b). When redeployed a day later near the drifter, CFE-Cals 2 and 4 advected to the west but at a greatly reduced speed indicating that the upper 200 m had become decoupled from the faster flow tracked by CFE-1 and CFE-3. During L2a, ADCP data showed a consistent net west-north-west current velocity at 0.17 m s^{-1} in the upper

50 m, an increase to 0.29 m s^{-1} between 100 and 200 m, and 0.27 m s^{-1} between 200 and 300 m (Fig. 9(b)); CFE motions were used to infer a velocity of 0.15 m s^{-1} at 500 m. During L2b, the current direction was to the west, but velocities were reduced

360 at all depths (0.04 m s^{-1} in the upper 50 m, 0.11 m s^{-1} between 100 and 200 m, and 0.12 m s^{-1} between 200 and 300 m; Fig 9(c)).

3.1.3 Location 3

L3 was located 240 km offshore in transitional waters between the westward extending filament and the surrounding southerly flowing waters of the California Current. The MLD_{24} at L3 averaged 27 m (range 11-69 m). The euphotic zone was at least

365 twice as deep as the MLD_{24} (77 m NASA VIIRS; 49±7 m from PAR profiles, Table 2). The base of the euphotic zone was bounded by the σ_0 = 25.75 kg m^{-3} isopycnal. CFEs-1 and 3 and CFE-Cal-2 were launched but recalled within 24 hours for repositioning as CTD cast data indicated a relatively strong influence of the filament. CFE-3 was lost at this time. CFE-1 and CFE-Cals 2 and 4 were redeployed approximately 10 km to the south of first deployment locations.

Salinity of the upper 50 m at L3 decreased over time from 33.35 to less than 33.2 PSU indicating an increasing component of

370 the southerly-flowing low-salinity California Current water (Schneider, et al., 2005). Surface layer nitrate averaged 1.9 µM. CFE flux indicators were low (Fig. A-3(a)). Current flow was to the southeast at L3 with 0.30 m s^{-1} velocities in the upper 50 m, 0.14 m s^{-1} between 100 and 200m, and 0.08 m s^{-1} between 200 and 300m (Fig 9(d). CFE drift at 500 m was 0.07 m s^{-1}. CFE trajectories followed the path of the PIT array but at a slower speed.

3.1.4 Location 4

375 This site (235 km offshore) was located ~35 km north of L3 in the western extension of the filament (Figs. 3g, h). Based on the salinity signature of L2b and L4, the water masses were similar (Table 2, Fig. 10). SMPP-VIIRS chlorophyll data (Fig. A-3(b)) show low and nearly uniform chlorophyll (0.25 mg m^{-3}) in the vicinity of observations. Surface nitrate was depleted, and sea surface temperature had increased due to solar heating (Fig. 3h, Fig. 10). MLD_{24} averaged 9 m; euphotic depth was 51±6 m. The euphotic zone base corresponded to the σ_0 = 25.0 isopycnal. ADCP currents were to northeast at 0.11 m s^{-1} in the upper

380 50 m, decreasing to 0.04 m s^{-1} between 100 and 200m, and 0.02 m s^{-1} between 200 and 300 m; at 500 m, a velocity of 0.03 m s^{-1} was calculated from CFE drift displacements.

A reasonable assumption is that the average salinity of the surface layer (here defined as upper 20 m) at L2 and L4 is a result of binary mixing of recently upwelled L1 water with the California Current water at L3. Using data in Table 2, we calculate that surface waters at L2a were an 81.1:18.9 % mixture of L1 and L3 waters; similarly, L2b was 80.9:19.1 %, and L4 was

385 74:26 %. As the filament moved over 200 km offshore it remained mostly hydrographically distinct.

3.2 Sinking Particle Lateral Displacements

One of the questions raised in particle flux measurement is: How well are fluxes at depth related to measured surface layer export? As an exercise we consider particles sinking at a hypothetical rate of 100 m d^{-1} from 50 m to depths of 150, 250, and 500 m and their lateral displacements during sinking at the 4 locations. Figure 13 visualizes such displacements.

390   CFE positions followed a near linear trajectory in time at many locations despite drifting at different depths; trajectories were in close agreement with ADCP current velocities (Fig. 9). The linearity of track allows a simple calculation of displacements in the direction of motion. At L1, ADCP velocity data (discussed in Sect. 3.1) indicate that particles sinking at 100 m d^{-1} would lag behind the surface layer by 7 km as they transited from 50 m to 300 m. At L2a, particles leaving 50 m would lead the surface layer by 11 km by the time they arrived at 150 m; they would lead surface waters by total of 19 km by 250 m; particles

395   would lag the 250 m layer by 4.5 km on reaching 500 m. Taken together particles sinking from 50 m would have a net displacement of 15 km relative to the surface layer. At L2b, in a weaker current regime, sinking particles would lead the surface layer by 6 km during transit to 150 m and have a total displacement lead of 12.5 km by 250 m. At L3, in transitional waters, particles would lag behind the motion of surface waters by 14 km by 150 m, and lag surface waters by 83 km on arrival at 500 m. At L4, particles settling at 100 m d^{-1} would lag behind the 50 m layer by 3.5 km on reaching 150 m and would have a total

400   displacement of 13 km by 500 m.

In summary, inferred lateral displacements were calculated relative to the direction of flow of surface waters as particles sink from 50 m to deeper waters. Smallest net displacements of sinking particles were found at L1 (7 km, 300 m), L4 (13km, 500 m) and L2a (14 km, 500 m). Location L3 in the transitional waters had the strongest net displacements (83 km) by 500 m, making a 1D interpretation of particle flux most problematic at this location. An interesting feature of L2 is that particles at

405   depth would lead the surface layer. Displacements of particles sinking at a different velocity, V, would scale by 100/V.

Particle flux profiles observed by the CFEs may reflect heterogeneous sources over the scales of displacement. If spatial gradients of particle sources along the axis of the plume are weak, then the vertical lead and lag effects will be in effect smaller. SMPP-VIIRS chlorophyll fields provide a measure of mesoscale chlorophyll variability at Location L2. Imagery from June 14 during the early stages of sampling show chlorophyll varying over a range of 3 to 1.75 mg Chl m^{-3} along the path of the

410   profiling CFE's; Imagery from June 17 showed a variation of 2.5 to 1.75 mg Chl m^{-3} (Fig. 5b) along the same track. The two images for June 14 and 17, show ranges of 2.25 to 2.75 and 1.75 to 2.25 mg Chl m^{-3}, respectively in the vicinity of the later deployment of CFEs (waters referred to as L2b). If chlorophyll is a metric of particle flux, then spatially variable fluxes would be expected to vary by less than a factor of two at L2. Similar maps for L1, L3 and L4 (Appendix Figs. A1-1, A1-2 and A1-3) indicate the likelihood of heterogenous fluxes at L1 and L3, but minimal heterogeneity at L4.

3.3 Particle Classes and size dependent POC$_{ATN}$ fluxes.

420 Figure 14 shows representative CFE imagery (selected from the 1250 images) taken at the 4 locations at depths 70, 125, and 250 m at L1, and at depths of 150, 250, and 500 m at the other locations. The dominant class of particles contributing to export at each location varied. Shallow export flux through 100 m at L1 was dominated by 7–10 mm long optically-dense anchovy pellets (Fig. 14); at L2 copepod pellets (Fig 14; Fig. 6g, h; Fig 8a) accounted on average for 50% of the flux (range 10 % to 90 %; Fig. 7b) with >1000 μm aggregates (Fig. 6, Fig. 14) accounting for the rest. At L3 and L4, export was dominated at all

425 depths by >1000 μm sized aggregates. Large >1000 μm sized aggregates resembling discarded larvacean houses were common at all sites at depths 250 m and below. We infer their origin based on size and morphology. Such aggregates were also present in samples closer to the surface, though not typically as abundant.

Volume Attenuance Flux was converted to POC$_{ATN}$ flux (1 VAF unit = 1 mmol C m^{-2} d^{-1}, Sect. 2.2.2) and partitioned into 30-100 μm, 100-200 μm, 200-400 μm, 400-1000 μm, >1000 μm size categories for 21 CFE dives at the 4 locations. Martin curve

430 parameters were derived from linear least squares fit to the log$_{10}$ transforms of the data according to Equation 3:

$$\log_{10}F = b*\log_{10}(z/z_{Ref}) + \log_{10}(F_{Ref}).$$ (3)

F is POC$_{ATN}$ flux at depth z, b is the Martin power, and z$_{Ref}$ was set to 50 m at L1, and 100 m at L2, L3, and L4, respectively. F$_{Ref}$ is calculated from the intercept. It should be noted that Martin b values are independent of the reference depth chosen. As z/z$_{Ref}$ is precisely known, it is chosen as the X variable. Table 3 summarizes Martin fit results for POC$_{ATN}$ flux. Table 4

435 summarizes Martin parameters for PIT derived carbon flux (POC$_{PIT}$ flux) and to POC$_{PIT}$ flux combined with a new production-based estimate euphotic zone carbon export (POC$_{NP}$ flux) (Kranz et al., 2020, Stukel and Landry, 2020); z$_{Ref}$ was set to the euphotic zone depth. Table 5 is a tabulation of Martin fit results for particle number fluxes across the different size categories. Data used for regressions are provided as supplemental on-line material.

Figure 15a shows POC$_{ATN}$ flux for individual dives partitioned by particle size class. Martin fits to the data are also shown

440 (Table 3). Figure 15b shows the fraction of POC$_{ATN}$ flux for each size category. Large symbols denote pooled data at 4 depth horizons. POC$_{ATN}$ flux decreases with depth at all locations for particles in the 30-100 μm, 100-200 μm and 200-400 μm categories, often close to the classic Martin function (Table 3). Our refinement of the 200-400 μm fraction which separated the high-attenuation ovoid faecal pellets from other particles (Fig. 8) also shows that this pellet class consistently decreases down the water column at all locations. The >1000 μm POC$_{ATN}$ fluxes increase with depth at L1 and L2, and show little trend

445 with depth at L4, and a slow decrease with depth at L3. Flux was dominated by >1000 μm aggregates at all locations except at L2 near 100 m where 200-400 μm material had an equal contribution (Fig. 15b).

At L1, POC$_{ATN}$ flux was high with significant anchovy faecal pellet contributions (Fig 14). At location L2, the flux at 150 m was dominated by 200-400 μm sized olive-coloured ovoid faecal pellets. Number fluxes were 150,000 m^{-2} d^{-1}. Evidence suggesting a fast-sinking rate for these particles was that they accumulated at the edges of the sample stage reflecting the

focusing effect of the tapered funnel (Fig. 14, L2 at 150m); aggregates were more evenly distributed across the sample stage. At this depth, >1000 μm aggregates accounted for less than 0.5% of particle number flux but ~40% of attenuation flux. In deep

470 waters aggregates accounted for 95% of the flux. At L3, flux was lower overall but >1000 μm sized aggregates carried ~70% of attenuation flux at 150 m, with aggregate contribution increasing to 80% in deeper waters. At L4 >1000 μm sized aggregates carried about 85% of the particle flux at 150 m, increasing to >90% in deeper waters (Fig. 15b).

Note on particle size-distributions. During review, we were asked if the funnel of the CFE led to artificial aggregation of particles forming either the ovoid faecal pellets or >1000 μm aggregates and also if we can provide further evidence that the

475 ovoid faecal pellets and aggregates were relatively fast sinking.

Did the funnel design used by the CFE lead to biased size-distribution results? We have seen no evidence that the polished, electrically neutral, and steeply sloped titanium funnel used in the CFE played any role other than the physical focusing of fast-sinking faecal pellets at the edges of the sample stage. During post recovery inspections, we have not found any evidence of fouling of the funnel surface. We also note that successive images taken 20 minutes apart show that the ovoid particles

480 arrived individually (Bishop, 2020a) and that similar pellets and pellet number fluxes were noted in PIT gel–sediment trap samples at L2 (Connors, et al., 2018). The answer to the first question is no.

Are the particles fast sinking? The model of Komar et al. (1981) when applied to an average sized ovoid pellet (ECD = 250 μm, length/width ratio = 1.5; Figs. 6g and 8b), having an excess density relative to sea water of 0.2 g cm^{-3}, sinking through 10 °C water (viscosity = 0.0144 poise) would have a sinking velocity or 350 m d^{-1}; the smallest particle in this category (ECD=200

485 μm) would sink 200 m d^{-1}. For aggregates, we used the Bishop et al. (1978) modification of the broad-side sheet settling model of Lerman et al. (1975). An aggregate with an ECD of 1500 μm and net excess density of 0.087 g cm^{-3} would settle at 300 m d^{-1} (Bishop et al., 1978). For reasons outlined in Bourne et al. (2019) we believe the aggregate model may overestimate sinking speed, but by no more than a factor of three; so, 100 m d^{-1} is a reasonable lower limit. Henson et al. (1996) measured sinking rates for similarly sized aggregates and discarded larvacean houses to be ~ 120 m d^{-1}. Further evidence for fast sinking speeds

490 for the particles that contribute to flux comes from time series sediment trap deployments (e.g., 175-300 m d^{-1} from Wong et al. 1999 (station PAPA), and >190 m d^{-1} from Conte et al., 2001, Bermuda time series). The answer is yes.

3.4 Total POC$_{ATN}$ fluxes.

Figure 16 shows total POC$_{ATN}$ flux for individual dives and for pooled dive results at 4 depth horizons. Also shown are the POC$_{NP}$ and POC$_{PIT}$ fluxes. Curves are Martin fits to both individual dives and pooled POC$_{ATN}$ fluxes as well as to POC$_{PIT}$ flux

495 and combined POC$_{PIT}$ and POC$_{NP}$ fluxes. Highly variable fluxes were observed at L1, consistent with the temporarily variable contributions of anchovy faecal pellets and with satellite imagery showing strong gradients of surface chlorophyll. (Appendix A, Fig. A1-1). At L2, flux increases with depth. L4 had fluxes were as high as those observed at L1. Strongly reduced fluxes

were observed in the transitional waters of L3. The POC_{PIT} flux was in close agreement with POC_{ATN} flux near 100 and 150 m at L2 and at L4.

Total POC_{ATN} flux increased with depth at L2 from 12.4 mmol C m^{-2} d^{-1} at 150 m, to 28.3 mmol C m^{-2} d^{-1} by 250 m, and to 38 mmol C m^{-2} d^{-1} by 500 m (Fig. 16). At L3, in transitional waters outside the filament, POC_{ATN} flux varied with depth from 3.8 mmol C m^{-2} d^{-1} at 150 m, to 3.9 mmol C m^{-2} d^{-1} at 250 m and 2.4 mmol C m^{-2} d^{-1} by 500 m. At L4, flux at 150 m averaged 25 mmol C m^{-2} d^{-1} (range 5–72 mmol C m^{-2} d^{-1}). Interestingly, none of the locations showed a strong decrease of flux with depth as one would expect based of the traditional Martin curve (Fig. 16). POC_{ATN} fluxes at L1 follow a Martin b (95% confidence interval in parentheses) of +0.37 (±0.59), and L2 +0.85 (±0.31) show little change or increase with depth. Trends at L3 and L4 yielded b values -0.45 (±0.70) and -0.24 (±0.68), indicating flux trends that slowly decrease with depth; trends similar to those reported by Bishop et al. (2016).

3.5 Water Column POC

Transmissometer beam attenuation coefficient is a strong optical proxy for POC in the upper kilometre of the water column (Bishop, 1999; Bishop and Wood, 2008; Boss et al., 2015). Between 41 and 89 % of this signal is typically due to beam interaction with relatively small, slowly sinking particles (Chung et al., 1996; Bishop, 1999). Surface layer transmissometer-derived POC ranged from a high of 35 µM at L1, to a low of 2 µM at L4 (Figs. 11 and 12, Table 2).

The integrated standing stock of POC in the water column was highest nearest shore at L1 and progressively dropped with distance offshore (and time) in the filament (Fig. 10). At L1, where the sea floor was at 450 m, relatively high POC levels (averaging ~1 µM) were detected in the 300 m to 450 m interval, indicative of resuspended particles forming a bottom nepheloid layer. It is important to note that CFEs did not sample in the nepheloid layer.

4. Discussion

4.1 Circulation

When considering carbon export dynamics, especially in regions with strong current systems, it is essential to understand the vertical profile in the context of the physical environment. As mentioned previously, by June 20–25, a depression in sea surface height (SSH) roughly 100 km in diameter had developed about 200 km off the coast. Such a SSH depression indicates the formation of a cyclonic eddy as Ekman transport would yield a net transport out of the centre to the edge of the eddy as waters rotate clockwise around the centre. As CFEs are Lagrangian, they drift with currents at depth during deployments, and their positions over time can be used to infer current velocity (Sect. 3.2). The CFE trajectories from dives to 150 and 250 m all reinforce such counterclockwise motion, consistent with ADCP data (Fig. 4; Fig. 9). Waters at L1, located ~20 km from the coast, were strongly influenced by tidal motion but overall flowed offshore to the west. At L2, the water was flowing quickly

to the west-northwest. As this westward flowing water encountered offshore water flowing eastward, a cyclonic eddy formed, with anticyclonic eddies forming to the north and south. L3 was located outside of a developing cyclonic eddy, with water moving quickly to the south east. L4 was in slow moving waters close to the centre of the eddy. These large-scale circulation patterns, with consistent directionality of water flow traced by CFEs at all depths has implications for the flux profiles as 540 discussed in depth below.

4.2 Comparison with other studies

Siegel et al. (2014) estimated carbon fluxes carried by algal aggregates and zooplankton faecal matter at the base of the euphotic zone from a food web model driven by satellite observations including SST, chlorophyll a, net primary productivity and particle size for monthly climatological conditions. The Siegel et al. (2014) climatological flux for June in our region is shown in Fig.
545 17a. Recognizing the spatial coarseness of Siegel et al.'s 1x1 degree gridded data set, the model predicts a base of euphotic zone flux of about 20 mmol C m^{-2} d^{-1} near-shore, with progressively lower fluxes going offshore to values of around 5 mmol C m^{-2} d^{-1} at offshore L3. In order to compare CFE flux results at 250 m, these modelled euphotic zone export fluxes were extrapolated to 250 m using Eqn. (1) and the Martin b value of -0.83 reported by Martin et al. (1987) for the VERTEX 1 site (Fig. 2). POC$_{ATN}$ fluxes at 250 m are plotted in the figure and are higher in all cases except in the transitional waters at L3.
550 The point of this comparison is that filaments appear to make a disproportionately large contribution to carbon transfer to deeper waters and that such filaments need to be included in models.

One of the closest observations in terms of distance from coast, season, and span of the water column is the VERTEX–1 (V–1; Martin et al., 1987). Martin's station V–1, occupied in June 1984 in intense upwelling and high chlorophyll conditions, was located off the coast of Point Sur approximately 100 km north of L2 (Fig. 2). VERTEX deployed surface tethered particle
555 interceptor (PIT) sediment traps from 50 to 2000 m, similar to those deployed during CCE-LTER. V–1 fluxes at 50 and 100 m, were 25 and 19.6 mmol C m^{-2} d^{-1}. At L1, our CFE fluxes at 50 m and 125 m, were 21 and 50 mmol C m^{-2} d^{-1}, respectively. Although V-1, fluxes were similar to our results, the profiles in deeper waters diverged. Flux at L1 was nearly constant or slowly increasing with depth; and the flux at L2 increased with depth; in contrast, V-1 data decreased strongly. The comparison with VERTEX results is justified since Point Sur has been identified as an area of frequent filament development (Abbot and
560 Barksdale, 1991; Gangopadhyay et al., 2011); furthermore, chlorophyll fields mapped using the NASA Coastal Zone Colour Scanner in June 1984, although few, confirm a filament structure near V–1 at the time of sampling (Fig. A1-7).

There are two candidate explanations for why V–1 results, and our data taken in similar conditions display such different behaviours. First, L1 was located over a wide 500 m deep "shelf" and L2 offshore was down current of this feature, whereas V–1, in 3 km deep water, was offshore of a much narrower shelf (Fig. 2a). When high export occurs over a broad shelf,
565 particles can accumulate in a fluff layer near bottom and be resuspended in a nepheloid layer. Such a layer can clearly be seen

at L1 in both transmissometer derived POC and in water turbidity (Fig. 11) and thus there is a potential source of particles to offshore waters.

The second possible explanation is that many of the >1000 μm sized aggregates seen in CFE imagery would be excluded from surface tethered baffled PIT traps due to 'baffle bounce' (Bishop et al., 2016), observed when currents relative to the trap are faster than 0.02 m s^{-1}. Stated another way, the size scale of the aggregates relative to the cm-scale baffle opening on traps, coupled with a near horizontal encounter with the trap opening would cause aggregates to bounce back into the flow and thus not be sampled. This was observed using surface tethered OSR instruments during quiescent conditions in the Santa Cruz Basin (Bishop et al., 2016). In our observations of the relative behaviour of PITs and CFEs, relative current speeds across the PITs were generally faster than this threshold. While smaller particles at L2 did attenuate with depth, aggregate fluxes increased (Fig. 15a), thus there is support for this hypothesis.

Surface–drogued PIT traps were deployed at 50, 100, and 150 m during the CCE-LTER study (Kranz, et al. 2020). At 150 m at L1, L2 and L4, trap measured flux and CFE derived fluxes (Fig. 16) were in relatively close agreement. At L3 in transitional waters, PIT trap fluxes at 150 m were two times higher than CFE results; however, the strong surface current regime encountered there rapidly separated the two observing systems spatially. Based on the reasonable agreement of results, the second candidate explanation is disfavoured.

In Sect. 2.2.4 we investigated sources of error. We concluded that the 9% uncertainty in the VAF: POC flux relationship and its assumed constancy with depth is not a factor in the interpretations that follow. The contribution of counting errors to POC_{ATN} flux in the 1000–10000 μm size category, are small at locations L1, L2, and L4 do not change our main conclusions below; errors in POC_{ATN} flux are illustrated in Appendix A Fig A1-5b.

If trap fluxes from 50, 100, 150 are fit with a Martin function, does the extrapolated curve adequately match POC_{ATN} fluxes deeper in the water column? Figure 16 depicts POC_{PIT} and POC_{PIT} + POC_{NP} fluxes extrapolated to depth using the Martin regression applied to 50-150 m results (data in Table 4). At L1, L2, L4, and L3 Martin b values (95% confidence interval in parentheses) were -0.37 (±0.27), -0.86 (±0.22), -0.30 (±0.19), and -2.01 (±0.51), respectively; 3 of 4 regressions are significantly different (at >95% confidence) from Martin. Fits combining POC_{PIT} and POC_{NP} fluxes yield b values of -0.78 (±0.34), -1.11 (±0.26), -0.16 (±0.26), and -2.02 (±0.41) for L1, L2, L4, and L3 (respectively). In this case, L3 and L4 remain significantly different from classic Martin curves. At 300 m (L1) and at 500 m (L2 and L3), POC_{PIT} Martin extrapolated fluxes would fall lower than CFE fluxes by factors of 2.1, 6.8, and 4.9. Only at L4 did fluxes agree well. The first take away is that Martin b factors are rarely 'Classic' and often are substantially lower than expected. The second, take away is that the mismatch (POC_{PIT} extrapolated vs. POC_{ATN} observed) indicates that fundamental processes contributing to the flux profile are not accounted for by the Martin relationship in deeper waters.

Considering the two candidate explanations above, we hypothesize that some ecological or physical process linked to a wide-shallow continental margin environment leads to more efficient transfer of POC through the water column in the CCE_LTER study case. More work on the intercomparison of PIT traps and CFEs, particularly particle classes sampled, would resolve any sampling bias issues. While mesoscale (4km) chlorophyll variability (Sect. 3.1; Fig. 5b) at L2 was small, there is no insight regarding the variability of particle flux from these observations.

4.3 Mechanisms for Non-Classic Martin Behaviour

In the CCE_LTER process study reported here, we do not observe total POC$_{ATN}$ flux attenuating with depth deeper than 100 m at any of our locations. At two locations we see flux near constant or increasing with depth. At other locations we observe flux decreases with depth at a rate slower than predicted by the Martin formulation. We explore reasons why the flux profile from the coastal station VERTEX1 (Martin et al., 1989, Fig. 1), which follows the classic curve, differs from results of this study. In the following discussion, we use the term "non-classic" to represent such behaviour.

Figure 18 depicts four mechanisms which could explain why particle flux profiles may diverge from traditional Martin-like behaviour: (1) non-steady state flux and/or remineralization (Giering et al., 2016); (2) inputs from migratory organisms at depth (Turner, 2015, Bishop et al., 2016); (3) physical subduction of surface material along isopycnal surfaces (Omand et al., 2015, Stukel et al., 2018); (4) lateral horizontal transport of resuspended particles from the continental margin followed by aggregation and sinking (Pak et al., 1980, McPhee-Shaw et al., 2004, Chase et al., 2007, Alonso-Gonzalez et al., 2009).

4.3.1 (M1) Non-Steady State Flux

The Martin et al. (1987) formula assumes a steady state over the several days required for particles to transit from the base of the euphotic zone to mesopelagic depths (500 m in our case); however, CCE-LTER sampled a rapidly evolving system. Upwelled coastal water can spawn productive filaments and eddies that persist shorter than a month. Giering et al. (2016) describe cases, especially associated with bloom scenarios, where the water column may not be in steady state. Figure 19 depicts two such scenarios in which export and remineralization are time varying in a way that leads to an apparent non-varying flux with depth or to an increased flux with depth.

Non-steady state blooms and time variable changes of b factor can lead to inverted flux profiles as there is a temporal lag between peak export from the surface layer and the arrival of particles at depth (Figs. 18a and 19). One indicator of a temporal delay scenario would be finding ungrazed intact phytoplankton from a prior bloom at depth. CTD Chlorophyll fluorescence data, however, show no evidence of sinking ungrazed phytoplankton (Figs. 11 and 12). Furthermore, there is also no major trend of flux either increasing or decreasing with time at L2 (Fig. 5). That particle flux at 250 m L4 was 2.5 times higher than measured new production provides some support for the non-steady state flux mechanism at L4.

4.3.2 (M2) Efficiency of Grazing Community and Active Transport

Zooplankton are highly important to POC export as their faecal pellets or feeding webs package smaller non-sinking phytoplankton and particles; however, flux due to zooplankton produced faecal pellets and aggregates is highly dependent upon the zooplankton community present (Turner, 2015; Bishop et al.,1986; Boyd et al., 2019). Furthermore, the community of phytoplankton that develop seasonally and during the course of a bloom can have great impact on how surface material is exported to the mesopelagic.

High levels of production and biomass do not necessarily imply high export (Bishop et al., 2004, 2016; Lam and Bishop, 2007). In a multi-cruise study in the Santa Cruz Basin south of the CCE-LTER study area, Bishop et al. (2016) found that highest export levels coincided with lowest levels of surface chlorophyll. None of the POC_{ATN} flux profiles from the cruises (January 2013, March 2013 and May 2012) were traditional Martin curves. High levels of productivity, combined with efficient grazing and weak remineralization likely combined to create the conditions of very high flux (but low surface chlorophyll) observed in January 2013 (Bishop et al., 2016).

Vertical migrators can also transport material to depth (Fig. 18b). Diel vertical migrators such as euphausiids, salps and copepods consume material at the surface during feeding times, and then can excrete material when they retreat to depth (Steinberg et al., 2008). Fish can also transport consumed material to depths far below the euphotic zone.

Some heterotrophs produce faecal material that is much more efficient at being exported from the euphotic zone. Organisms such as krill and fish produce large dense faecal pellets which sink very efficiently. At L1, the near constant flux with depth was due in large part to fast sinking anchovy pellets. It has been reported that both copepod (Smetacek, 1980; Krause, 1981; Bishop et al., 1986; Bathmann et al., 1987; Gonzalez et al., 2000) and protozoan (Gonzalez, 1992b; Beaumont et al., 2002) pellets do not have high transfer efficiency on sinking from the euphotic zone. Gonzalez (2000) found only 0.1-2.5% of copepod faecal pellets in the upper 100 m Humboldt current reached sediment traps at 300m. The fast recycling of copepod faecal pellets in the surface has been attributed primarily to coprophagy (Beaumont et al., 2002; Smetacek, 1980). Evidence suggests that the fast recycling of zooplankton pellets in the epipelagic is due to the activities of other zooplankton (Turner, 2015 and references therein). There are a number of zooplankton known to eat faeces (coprophagy) including radiolarians (Gowing et al., 1989), tunicates (Pomeroy et al., 1984) and copepods (Sasaki et al., 1988).

At L2 at 150 m, 200-400 μm sized ovoid pellets were very abundant and were fast sinking. The ovoid pellet number flux at 150 m was 150,000 m^{-2} d^{-1}; however, by 500 m, the pellets flux was reduced a factor of 20 (Fig. 8a), These trends were confirmed and calibrated by manual particle counts (Connors et al., 2018). The membrane-bound small ovoid pellets were olive coloured (Fig. 6g) and shown in SEM imagery to be full of diatom frustules and fragments as were the anchovy pellets at L1 (Fig A1-6). At L3 and L4, the pellet flux decreased from 100 m to 500 m by factors of 8 and 5, respectively; at L1 the decrease was 2.5-fold between 50 and 250 m (Fig. 8c).

At L2, as the ovoid pellets decreased with depth, the concentration of aggregates, many of which closely resemble discarded larvacean houses, increased to dominate POC$_{ATN}$ (Fig. 15b). Larvaceans produce fine mucous feeding webs that concentrate and ingest particles from 0.2 to 30 μm in diameter (Gorsky and Fenaux, 1998). Typically, a larvacean feeds on only a fraction of the material in their web before it discards it due to clogging (Berline et al., 2011); furthermore, some larvaceans create and discard up to 26 feeding webs a day (Sato and Tanaka, 2001). They therefore can be major contributors to carbon flux. Larvaceans are found throughout the upper 1000 m (Stemmann et al., 2008) and they are often the most abundant mesozooplankton after copepods (Gorsky and Fenaux, 1998). Larvaceans with intact feeding structures are difficult to study as they are fragile, and therefore difficult to capture in either plankton nets (Berline et al., 2011; Silver et al., 1998). The larvaceans without houses are captured in net tows; however, newly reported results from *Zooglider*, an autonomous buoyancy driven glider with interfaced zooplankton imaging system, showed order-of-magnitude higher abundances of larvaceans compared simultaneous MOCNESS collections during operations in the vicinity of the La Jolla canyon in March 2019 (Whitmore, et al., 2019). It is clear that the full impacts on flux by migratory communities and their modification of sinking particle flux is, at yet, only partly realized.

Vertical migration likely does contribute export to depth. At L2, we did see evidence of migration to 250 m in preliminary biomass profiles from MOCNESS tows (Ohman, personal communication, July 2020) and in ADCP scattering intensity records. However, the increase of flux with depth cannot solely be explained through transport of material from the surface to depth through vertical migration. For one, vertically migrating crustacean species in the CCE have a gut turn over time of about 30 minutes, thus in 1-2 hours to swim to depth only 50% or 25% of excreted material would be delivered to 250 m, where we see increased flux. The aggregates at depth are clearly not aggregations of faecal pellets. This does not rule out that vertical migrators were important, as gelatinous organisms such as larvaceans and salps have been known to migrate daily. A quantitative analysis of the CCE–LTER MOCNESS speciation and of multifrequency fisheries echo sounder data would help resolve these questions but has yet to be performed.

Does active transport explain the flux increase at L2? At L2, Kranz et al. (2020) report POC$_{NP}$ export flux of 101.6 ± 44.0 mmol C m^{-2} d^{-1}. In close agreement with our calculated export flux of ~120 mmol C m^{-2} d^{-1} for the 9-day period between studies at L2a and L4 (Sect. 2.4). Sinking particles are consumed by particle grazers and assimilation efficiency can vary by species and food substrate. Previous work has reported that salps have a 61% assimilation efficiency for carbon (Madin and Purcell, 1992). If exported particles were processed using this efficiency, and if all particles were consumed by vertically migrating organisms and excreted at depth, there would be a flux of 48 mmol C m^{-2} d^{-1}. The same calculation assuming an assimilation efficiency of 90%, would add ~12 mmol C m^{-2} d^{-1} at depth. Flux at 500 m at L2 was 38 mmol C m^{-2} d^{-1} which would require dominant migratory inputs. While vertical migrators, are likely important contributors to flux, their activities may not fully explain the depth increasing flux profiles observed at L2. It is clear that the flux carried by aggregates at depth cannot form from the coprophagy of sinking faecal pellets.

4.3.3 (M3) Physical Subduction

In most regimes, export of particulate organic carbon (POC) to depth is primarily attributed to sinking particles; however, in dynamic regimes sub-mesoscale eddy driven flux may be responsible for transporting a significant percentage of living phytoplankton along isopycnal surfaces to depth (Omand et al., 2015; Fig 18c). The filament we followed produced a cyclonic eddy with divergent surface water flows, which would have led to upwelling, not downwelling. While subduction of ungrazed phytoplankton may also occur at fronts; there is no evidence to support a subduction process connecting the surface layer to 250 m at L2 as chlorophyll fluorescence profiles (Fig. 11) show minimal presence of phytoplankton material deeper than 100 m. Spatial transects across the filament furthermore showed little evidence of fluorescent particles deeper than the $\sigma_\theta = 26.0$ kg m^{-3} isopycnal at 100 m (Fig. 12). Our findings are consistent with those of Stukel et al. (2018) who found in targeted study of fronts in the CCE region that subducted particles were completely remineralized by 150m. Eddy driven subduction and frontal subduction processes do not play a role in fluxes seen in our data.

4.3.4 (M4) Lateral Advection

Turbulent currents interacting with continental shelf and upper slope sediments can pick and transport sediment and fluff layer material offshore along isopycnals (Fig. 19d). Along the flow path filter feeding organisms can consume the particles and produce sinking material adding to vertical flux and thus increase POC flux at depth. The California Current eastern boundary regime is typical of such conditions. Intermediate nepheloid layers found at several hundred meters depth off the coast of Oregon were tracked to a continental shelf sediment origin (Pak et al., 1980). Similar layers have been observed between 70 and 150 m on the outer continental shelf off northern California (McPhee-Shaw et al., 2004). In a box model study of Canary Current region, Alonso-Gonzalez et al. (2009) calculated that lateral suspended POC fluxes of continental shelf origin were up to three orders-of-magnitude greater than vertical fluxes. Their results suggest that laterally sourced POC could be a significant part of the mesopelagic carbon current budget in their study area. If their model is applicable to other eastern boundary current regimes, then lateral sourced POC transport may play a crucial role in global carbon cycle.

Kelly et al. (2018) found an inverse relationship with higher e-ratios (export at euphotic zone base/net primary productivity) in offshore regions and lower e-ratios in the more productive coastal regions over 5 CCE cruises. Furthermore, a strong correlation between sea surface temperature and export was found, which they determined not to be causal, but rather an effect of lateral advection bringing upwelled, cold productive waters offshore.

Observed nepheloid layers near L1 might indicate that lateral transport could be a possible factor explaining flux increase with depth at L2 in our study. Support for this comes from the finding of strong offshore currents at L2 (Figs. 9b and c). During the first two days of the CFE deployment, transports were to the west-northwest, with velocities averaging 0.2 m s^{-1} between 100 and 300 m. CFE trajectories during 500 m dives indicate that deeper water was also moving in the same direction (Fig. 9). The offshore flowing currents, if carrying a high concentration of non-sinking POC derived from the shallow continental margin

Deleted: 201

Deleted: While,

Deleted: 100 m deep

Deleted: surface

Deleted: E

Deleted: therefore did

Deleted: ¶

Deleted: north-west

near L1 could supply a substrate for particle gazers at depth. Alternatively, Large aggregates sourced shallow in the water column between L1 and L2 could be present in deeper waters at L2a and thus explain the apparent increase of flux with depth at L2.

On the other hand, several points of evidence argue against lateral transport and repackaging of nepheloid or fluff layer material as contributing to POC_{ATN} flux at L2. First, the nepheloid layer is seen at L1 in the 300–450 m interval (average POC = 1.4 µM; Fig. 11) and a similar intermediate nepheloid layer found at L2a between 50 and 250 m occurs in waters of very different density; the nepheloid layer at L1 occurs in waters with a σ_θ range of 26.7–26.92 kg m^{-3}, whereas the L2a layer is found in waters with σ_θ ranging from 26.1–26.7 kg m^{-3}; the feature is absent at L2b (Fig. 12). Secondly, UVP5-hd data shows that the nepheloid layer at L1 is dominated by smaller particles and not >1000 µm sized aggregates. In fact, in the 100-300 m depth interval there were fewer >1000 µm aggregates at L1 than at L2, and aggregates had identical concentrations below 300 m (Fig. 20). This rules out a direct connection involving the advection of large aggregates or resuspended small particles from L1.

4.3.5 Recap of flux mechanisms

We are left with a puzzle. All small particle classes smaller than 400 µm exhibit a decrease with depth at all locations consistent with a single origin within the euphotic zone and progressive particle remineralization during sinking. At the same time >1000 µm aggregate fluxes either increase with depth (L1 and L2) or slowly decrease (L3 and L4); the increased flux cannot be supplied by biologically mediated consumption and repackaging of the smaller sized sinking particles because the fluxes of <1000 µm particles are too low. Our strongest candidate mechanism to explain the >1000 µm POC_{ATN} flux profile at L1 & L2 is active transport (M2) or some related process transforming the DOC pool to POC flux at depth. Due to the strong decline in measured new production at L4, non-steady steady state export (M1) may have been an additional contributing factor at L4. The subduction (M3) and lateral transport (M4) mechanisms are disfavoured.

4.4 Anchovy Faecal Pellets; Enhancement of Carbon and Phosphorous Transfer Efficiency.

As noted in Sec. 3.3 above, Anchovy pellets were major contributors to flux at L1. Previous research has found that these large and dense faecal pellets sink at 750 m d^{-1} and are very efficient transporters of organic matter to deeper ocean. (Saba and Steinberg, 2012). SEM imagery of anchovy pellets sampled by CFE-Cal showed that the anchovies were primarily grazing on diatoms (Fig A1-6). Another indication of the efficiency of transport comes from the analysis of phosphorus and organic carbon in CFE-Cal samples (Bourne et al., 2019). Anchovy pellet dominated samples collected using the CFE-Cal at L1 had an organic carbon to phosphorus (C:P) ratio of 60:1, much lower than typical 300:1 ratio found in other samples; P is known to be lost rapidly relative to organic carbon from sinking particles (Collier and Edmond, 1984). Not only are anchovies primary grazers and thus potentially strong contributors to flux, they also appear to be enhancing the vertical transfer of phosphorus relative to carbon to the deep sea.

5. Conclusions

Coastal upwelling regions are disproportionately productive relative to their total surface area due to high levels of available nutrients. Four Lagrangian Carbon Flux Explorers (CFE) were deployed a total of two dozen times during the June 2 through July 1, 2017 California Current Ecosystem – LTER process study of a dynamic filament of productive water as it moved from the coast to the open ocean.

The CFEs provided an unparalleled view of particle flux and particle flux size distribution (30 μm to cm scale) within that system. In all environments, flux was dominated by particles >200 μm in size. At L1, >1000 μm anchovy pellets dominated. At L2, 200-400 μm sized olive-coloured ovoid pellets contributed on average ~50% of the flux and at times accounted for 100% of the flux at 100 to 150 m. At all locations, >1000 μm sized amorphous aggregates dominated flux at depths greater than 150 m.

We found during the CCE-LTER study that flux does not decrease with depth following a typical Martin power law (b= -0.86) relationship in many instances. Extrapolating POC flux from the euphotic zone to depth using the classic Martin curve in such productive regions strongly underestimates flux. Interestingly, flux profiles for particle classes smaller than 400 μm, always had negative b factors which were more closely in agreement with the classic Martin fit.

In this study of particle fluxes from 100 m to 500 m, the highest flux was found at L1, where surface chlorophyll initially exceeded >10 mg m^3. However, the magnitude of flux did not always correlate with surface chlorophyll. L4 had nearly the same flux, though surface chlorophyll was 50 times lower than at L1. We confirm the Bishop et al. (2016) conclusion that surface chlorophyll in the California coastal environment is a poor indicator of flux at depth. The efficiency of export was clearly affected by trophic structure as evidenced by the dominant particles contributing most of vertical carbon flux. At L1, flux was very efficient as anchovies directly grazed on primary producers, and produced dense phosphorus-rich, fast sinking pellets. At L2, though copepods were ubiquitous higher in the water column and their faecal pellets an important contributor to flux at 150 m, the contribution had largely disappeared by 250 m depth. At all locations the ovoid faecal pellet fluxes decreased as expected with increasing depth (Fig. 8) consistent with their production in or just below the euphotic zone and progressive loss with depth. Their pellets were not significant contributors to carbon flux deeper in the mesopelagic.

At L2, and to some extent at L1, there was a shift from faecal pellets near the surface to large aggregates at depth. At L3 and L4, large aggregates dominated POC flux at all depths. These aggregates resembled discarded larvacean feeding webs although they may have other origins. There was no direct evidence that westward moving currents laterally transported waters with POC or aggregates from the continental margin.

The flux profiles observed at most locations were unlike the classic Martin curve. As mentioned previously, the VERTEX–1 site in the classic Martin et al. (1987) study was located 100 km north of our L1 and L2 study areas and took place under similar conditions (including active upwelling and the presence of a filament). This study has found high fluxes and transfer

efficiencies through the mesopelagic zone, similar to observations in the nearby Santa Cruz Basin (Bishop et al., 2016). Both regions are adjacent to wide shallow shelves, whereas the observations of Martin et al. (1987) took place near a narrow shelf (Fig. 2). Shelf width is implicated in the supply of bioavailable iron to surface water phytoplankton communities (Johnson et al., 1999, Chase et al., 2007, Lam et al. 2008) with narrow continental shelf regimes being more iron limited. We use the analogy to iron supply to raise the question of whether flux profile differences are the result of intrinsic differences in the zooplankton/fish community composition, grazing and migratory behaviour, or food web structure in offshore waters near narrow vs. wide continental shelves?

At this writing, we are unable to fully explain the particle flux increase at L2 between 100 and 500 m, and we have not closed the story of the origins of the aggregates that dominate flux in all waters deeper than 150 m. This study shows that there are many new questions pertaining to filament dynamics and POC flux.

Fluxes made with surface–drogued PIT traps were generally in agreement with CFE fluxes near 100 and 150 m, suggesting that discrimination against >1500 μm aggregates as proposed by Bishop et al. (2016) may not be as important in the strong upwelling and wave conditions encountered during the CCE-LTER study; however, extrapolation of 50 to 150 m PIT fluxes to depth using Martin fits, led to significant (factors of 3 to 7) underestimation of flux at the deepest depth horizon sampled by CFEs again raising the question of how the deep aggregate populations and fluxes are achieved.

Unlike sample collecting devices (including CTD/rosettes, drifters, surface drogued sediment traps, and CFE-Cals) that must be ship-deployed, CFEs have a mission capability of 8 months of hourly operations (or 16 months at 2 hours …) and have been deployed for missions up to 40 days without compromise; the CFEs have been proven in a wide range of sea states and to depths of 1000 m (Bishop et al., 2016). Due to the complexities of particle size distribution and particle class measurement, which is not yet implemented on the CFE, all deployments have been tended by ships to date. The framework provided by the CCE-LTER process study provided an opportunity to advance towards full CFE autonomy while supporting science. Our hybrid size distribution analysis scheme provided key insights that are an important step towards fully autonomous operations in the global ocean. Both methods 1 and 3 (after modification) would be possible to run on the CFE during deployment.

In coastal regions, carbon export needs to be understood both laterally and vertically. A future expanded scope of autonomous observations during process studies and surveys would provide a 3D view of mechanisms dictating export in these regions and inform the new class of eddy resolving simulations of biogeochemical processes in the California Current System such as recently described by Deutsch et al. (2020).

Data Availability. Carbon Flux Explorer original transmitted light imagery and derived attenuance imagery (~1600 images each) and tabular size-analysis results from these images is archived at the Biological and Chemical Oceanography Data Management Office at Woods Hole Oceanographic Institution (Bishop, 2020a; Bishop, 2020b). The sources of all other data are identified in the text.

Author Contributions. HLB as part of her Ph.D. dissertation, played lead role in precruise laboratory preparation and CFE system assembly and testing; at sea HLB was science lead on deployment and recovery of CFEs; post cruise HLB led laboratory analysis of samples; she developed fast algorithms capable of running on the CFE in real time and codes that provided physical and hydrographic context for our observations; she developed the interpretive template for this manuscript. JKBB served as advisor to HLB during her Ph.D. dissertation and was PI of the project; at sea he maintained CTD-deployed particle concentration sensors and performed all CTD particle optics data reduction, he served as a third hand during CFE deployments and recoveries; post cruise he developed the hybrid particle size analysis codes and analysed remote sensing data sets; and worked to bring the paper to publication. TJW was lead on all engineering activities for CFE systems and their precruise ballasting; at sea, he maintained the CFEs and closely worked with HLB on CFE deployments, operations, and recoveries. ELC performed size distribution analysis of aggregates and pellets used validate the refinement of a pellet classification scheme developed by JKBB.

Acknowledgements. We would like to thank Mark Ohman (chief scientist), Mike Stukel (USF), members of the science party, and the captain and crew of the R/V Revelle for support during the 2017 CCE-LTER process study. Tim-Lowe (LBNL, Engineering – design lead) and Lee-Huang Chen (UC Berkeley, Engineering) contributed substantially to project success. We thank Mark Ohman for inviting us to sea and Mike Stukel for feedback and discussion of this manuscript. We also thank Alejandro Morales (LBNL) and Mike McLune (SIO – Instrument development group). Many UC Berkeley undergraduates aided in CFE related activities at sea and in the laboratory, in particular we thank Casey Fritz, Xiao Fu, Sylvia Targ, Jessica Kendall-Bar and William Kumler. We thank both reviewers for their contributions. US National Science Foundation grants OCE 1538696 and OCE 1724495 supported development of both CFE and CFE-Cal systems, HLBs thesis research, and seagoing activities. CCE-LTER project (including ship time) was supported by NSF OCE 1637632.

References

Abbot, M.R. and Barksdale, B.: Phytoplankton Pigment Patterns and Wind Forcing off Central California. Journal of Geophysical Research, 96(C8), 14,649–14,667, doi:10.1029/91JC01207, 1991

Alonso-González, I. J., Arístegui, J., Vilas, J. C., and Hernández-Guerra, A.: Lateral POC transport and consumption in surface and deep waters of the Canary Current region: A box model study, Global Biogeochem. Cycles, 23, GB2007, doi:10.1029/2008GB003185, 2009.

Bacon, M. P., Cochran, J. K., Hirschberg, D., Hammar, T. R., and Fleer, A. P. (1996). Export flux of carbon at the equator during the eqpac time-series cruises estimated from ^{234}Th measurements. Deep-Sea Research Part II: Topical Studies in Oceanography, 43(4–6), 1133–1153. doi:10.1016/0967-0645(96)00016-1, 1996.

905 Banse, K.: Reflections About Chance in My Career, and on the Top-Down Regulated World. Annual Review of Marine Science, 5(1), 1–19. doi:10.1146/annurev-marine-121211-172359, 2013.

Bathmann, U.V., Noji, T.T., Voss, M., and Peinert R.: Copepod fecal pellet: abundance, sedimentation and content at a permanent station in the Norwegian Sea in May/June 1986. Mar. Ecol. Prog. Ser., 38, 45-51. doi:10.3354/meps038045, 1987.

Beaumont, K. L., G. V. Nash, and Davidson, A. T.: Ultrastructure, morphology and flux of microzoo- plankton faecal pellets
910 in an east Antarctic fjord, Mar. Ecol. Prog. Ser., 245, 133–148. doi:10.3354/meps245133, 2002.

Berline, O., Stemmann, L., Lombard, F., and Gorsky, G.: Impact of appendicularians on detritus and export fluxes : a model approach at DyFAMed site, Journal of Plankton Research, 33(6), 855–872 doi:10.1093/plankt/fbq163, 2011.

Bishop, J.K.B., D.R. Ketten and J.M. Edmond: The chemistry, biology and vertical flux of particulate matter from the upper 400 m of the Cape Basin in the S.E. Atlantic Ocean. Deep-Sea Research. 25, 1121-1161. https://doi.org/10.1016/0146-
915 6291(78)90010-3. 1978.

Bishop, J.K.B.: Regional extremes in particulate matter composition and flux: effects on the chemistry of the ocean interior. In Berger, W.H., Smetacek, V.S., and Wefer, G. eds., Productivity of the ocean present and past. Dahlem Konferenzen. Chichester: John Wiley and Sons Ltd.. pp 117–137, 1989

Bishop, J.K.B.: Transmissometer Measurement of POC. Deep-Sea Research I. 46(2) 353-369. doi:10.1016/S0967-
920 0637(98)00069-7, 1999.

Bishop, J.K.B.: Original transmitted-light imagery and processed attenuance images of sinking particles observed by autonomous Carbon Flux Explorers deployed 100-500m in the California Current Regime, during the CCE-LTER process study (P1706) between June 2 and July 1, 2, 2017. Biological and Chemical Oceanography Data Management Office (BCO-DMO). (Version 1) Version Date 2020-09-17, 2020a. http://lod.bco-dmo.org/id/dataset/825076,
925 https://doi.org/10.26008/1912/bco-dmo.825076.1

Bishop, J.K.B.: Size fractionated Particulate Carbon Flux 100-500 m measured by autonomous Carbon Flux Explorers deployed during the CCE-LTER process study (P1706) between June 2 and July 1, 2017 in the California Current Regime. Biological and Chemical Oceanography Data Management Office (BCO-DMO). (Version 1) Version Date 2020-09-16, 2020b. http://lod.bco-dmo.org/id/dataset/823408. https://doi.org/10.26008/1912/bco-dmo.823408.1

930 Bishop, J.K.B. CTD profile data from Carbon Flux Explorers deployed 100-500m in the California Current Regime, during the CCE-LTER process study (P1706) between June 2 and July 1, 2017, 2020-09-30, 2020c http://lod.bco-dmo.org/id/dataset/825602. https://doi.org/10.26008/1912/bco-dmo.825602.1

Bishop, J.K.B., Wood, T. J., Davis, R. E., and Sherman, J. T.: Robotic observations of enhanced carbon biomass and export at 55 degrees during SOFeX, Science, 304(5669), 417–420. doi:10.1126/science.1087717, 2004.

935   Bishop, J. K. B., and Wood, T. J.: Particulate matter chemistry and dynamics in the twilightzone at VERTIGO ALOHA and K2 sites. Deep-Sea Research Part I: Oceanographic Research Papers, 55(12), 1684–1706. doi:10.1016/j.dsr.2008.07.012, 2008

Bishop, J. K. B., and Wood, T. J.: Year-round observations of carbon biomass and flux variability in the Southern Ocean. Global Biogeochemical Cycles, 23(2), 1–12. doi:10.1029/2008GB003206, 2009.

Bishop, J. K. B., Fong, M. B., and Wood, T. J.: Robotic observations of high wintertime carbon export in California coastal
940   waters. Biogeosciences, 13(10), 3109–3129. doi:10.5194/bg-13-3109-2016, 2016.

Bourne, H. L.: Marine Biogeochemical Cycling of Carbon and Cadmium. Ph.D. dissertation, University of California, Berkeley, 121 pp., 2018.

Bourne, H. L., Bishop, J. K. B., Wood, T. J., Loew, T. J., and Liu, Y.: Carbon Flux Explorer optical assessment of C, N and P fluxes, Biogeosciences, 16, 1249-1264, doi:10.5194/bg-16-1249-2019, 2019.

945   Boss, E., Guidi, L., Richardson, M.J., Stemman, L., Gardner, W.D., Bishop, J. K. B., Anderson, R.F. and Sherrell., R.: Optical techniques for in-situ characterization of particles pertinent to GEOTRACES. Progress in Oceanography. 133, 43–54. Doi:10.1016/j.pocean.2014.09.007. 2015.

Boyd, P. W., and Trull, T. W.: Understanding the export of biogenic particles in oceanic waters: Is there consensus? Progress in Oceanography, 72(4), 276–312. doi:10.1016/j.pocean.2006.10.007, 2007.

950   Boyd P. W., Claustre, H., Levy, M., Siegel, D. A. and Weber, T.: Multi-faceted particle pumps drive carbon sequestration in the ocean. Nature, 568, 327-335. doi:10.1038/s41586-019-1098-2, 2019.

Buesseler, K. O., Lamborg, C. H., Boyd, P. W., Lam, P. J., Trull, T. W., Bidigare, R. R., et al.: Revisiting carbon flux through the ocean's twilight zone, Science, 316, 567–571. doi:10.1126/science.1137959, 2007.

Burd, A. B., Hansell, D. A., Steinberg, D. K., Anderson, T. R., Arístegui, J., Baltar, F., eaupré, S. R., Buesseler, K. O., DeHairs,
955   F., Jackson, G. A., Kadko, D. C., Koppelmann, R., Lampitt, R. S., Nagata, T., Reinthaler, T., Robinson, C., Robison, B. H., Tamburini, C. and Tanaka, T.: Assessing the apparent imbalance between geochemical and biochemical indicators of meso- and bathypelagic biological activity: What the @$♯! is wrong with present calculations of carbon budgets? Deep Sea Research Part II: Topical Studies in Oceanography, 57(16), 1557–1571. doi:10.1016/j.dsr2.2010.02.022, 2010.

Chase, Z., P. G., Strutton, and Hales, B.: Iron links river runoff and shelf width to phytoplankton biomass along the U.S. West
960   Coast, Geophysical Research Letters, 316, 567–571, doi:10.1029/2006GL028069, 2007.

Chung, S.P., Gardner, W.D., Richardson, M.J., Walsh, I.D., and Landry, M.R.: Beam attenuation and micro-organisms: spatial and temporal variations in small particles along 140°W during the 1992 JGOFS EqPac transects. Deep-Sea Research II, 43, 1205-1226. doi:10.1016/0967-0645(96)00030-6, 1996.

Collier, R. and Edmond, J.M.: The trace element geochemistry of marine biogenic particulate matter, Progress in Oceanography, 13, 113–199. doi:10.1016/0079-6611(84)90008-9, 1984.

Connors, E.J., Bourne, H.L., and Bishop J.K.B.: Depth and Temporal Variation of Aggregate Export from the Biological Carbon Pump in Upwelling California Coastal Waters. Presented at the AGU/ASLO Ocean Sciences Meeting, Portland, OR, Feb. 2018. Poster BN14D-1059123, 2018.

Conte, M.H., Ralph, N. and Ross, E.H. Seasonal and interannual variability in deep ocean particle fluxes at the Oceanic Flux Program (OFP)/Bermuda Atlantic Time Series (BATS) site in the western Sargasso Sea near Bermuda, Deep Sea Research Part II: Topical Studies in Oceanography,48 (8–9), 1471-1505. 2001. https://doi.org/10.1016/S0967-0645(00)00150-8.

Deutsch, C., Frenzel, H., McWilliams, J. C., Renault, L., Kessouri, F., Howard, E., Liang, J-H., Bianchi, D., and Yang, S.: Biogeochemical variability in the California Current System. bioRxiv doi:10.1101/2020.02.10.942565, 2020. (on-line preprint).

Dunne, J. P., Armstrong, R. A., Gnanadesikan, A., and Sarmiento, J. L.: Empirical and mechanistic models for the particle export ratio. Global Biogeochemical Cycles, 19(4). doi:10.1029/2004GB002390, 2005.

Ebersbach, F., Trull, T.W., Davies, D.M., and Bray, S.G.: Controls on mesopelagic particle fluxes in the Sub-Antarctic and Polar Frontal Zones in the Southern Ocean south of Australia in summer-Perspectives from free-drifting sediment traps. Deep-Sea Research Part II: Topical Studies in Oceanography, 58(21–22), 2260–2276. doi:10.1016/j.dsr2.2011.05.025, 2011.

Eppley, R., Peterson, B.: Particulate organic matter flux and planktonic new production in the deep ocean. Nature 282, 677–680. doi:10.1038/282677a0, 1979.

Estapa, M. L., Siegel, D. A., Buesseler, K. O., Stanley, R. H. R., Lomas, M. W., and Nelson, N. B.: Decoupling of net community and export production on submesoscales in the Sargasso Sea. Global Biogeochemical Cycles, 29, 1266–1282. doi:10.1002/2014GB004913, 2015.

Gangopadhyay, A., Lermusiaux, P.F.J, Rosenfeld, L., Robinson, A.R., Calado, L., Kim, H.S., Leslie, W.G., and Hawley, P.J.: The California Current System: A multiscale overview and the development of a feature-oriented regional modeling system (FORMS). Dynamics of Atmospheres and Oceans 52. 131–169. doi:10.1016/j.dynatmoce.2011.04.003, 2011.

Giering, S. L. C., Sanders, R., Martin, A. P., Henson, S. A., Riley, J. S., Marsay, C. M., and Johns, D. G.: Particle flux in the oceans: Challenging the steady state assumption. Global Biogeochemical Cycles, 31(1), 159–171. doi:10.1002/2016GB005424, 2017.

Giering S. L. C., Cavan E. L., Basedow S. L., Briggs N., Burd A. B., Darroch L. J., Guidi L., Irisson J.-O., Iversen M. H., Kiko R., Lindsay D., Marcolin C. R., McDonnell A. M. P., Möller K. O., Passow U., Thomalla S., Trull T. W. and Waite A. M.:

Sinking Organic Particles in the Ocean—Flux Estimates From in situ Optical Devices. Front. Mar. Sci. 6,834. doi: 10.3389/fmars.2019.00834 2020.

González, H. E.: Distribution and abundance of minipellets around the Antarctic peninsula. Implications for protistan feeding behaviour, Mar. Ecol. Prog. Ser., 90, 223–236, doi:10.3354/meps090223, 1992.

González, H. E., Ortiz, V. C., and Sobarzo, M.: The role of faecal material in the particulate organic carbon flux in the northern Humboldt Current, Chile (23°S), before and during the 1997 – 1998 El Niño, Journal of Plankton Research, 22(3), 499–529, doi:10.1093/plankt/22.3.499, 2000.

Gorsky, G. and Fenaux, R.: The role of appendicularia in marine food webs, The Biology of Pelagic Tunicates, Oxford University Press, Oxford, 161–169, 1998.

Gowing, M.M.: Abundance and feeding ecology of Antarctic phaeodarian radiolarians, Marine Biology, 103, 107-118. doi:10.1007/BF00391069, 1989.

Gruber, N., Lachkar, Z., Frenzel, H., Marchesiello, P., Münnich, M., McWilliams, J. C., Nagai, T. and Plattner, G.-K.: Eddy-induced reduction of biological production in eastern boundary upwelling systems. Nature Geoscience, 4(11), 787–792. doi:10.1038/ngeo1273, 2011.

Henson, S. A., Sanders, R., Madsen, E., Morris, P. J., Le Moigne, F., and Quartly, G. D.: A reduced estimate of the strength of the ocean's biological carbon pump. Geophysical Research Letters, 38(4), 10–14. doi:10.1029/2011GL046735, 2011.

Johnson, K. S., Plant, J. N., Dunne, J. P., Talley, L. D., and Sarmiento, J. L.: Annual nitrate drawdown observed by SOCCOM profiling floats and the relationship to annual net community production. Journal of Geophysical Research: Oceans, 122(8), 6668–6683. doi:10.1002/2017JC012839, 2017.

Kelly, T.B, Goericke, R., Kahru, M., Song, M., and Stukel, M.R.: CCE II: Spatial and interannual variability in export efficiency and the biological pump in an eastern boundary current upwelling system with substantial lateral advection. Deep-Sea Research I, 140, 14-25. doi:10.1016/j.dsr.2018.08.007, 2018.

Komar, P.O., Morse, A.P., Small, L.F. and Fowler, S.W. An analysis of the sinking rates of copepod and euphausiid fecal pellets. Limnol. Oceanography. 26, 172-180,1981. https://doi.org/10.4319/lo.1981.26.1.0172.

Kranz, S. A., Wang, S., Kelly, T. B., Stukel, M. R., Goericke, R., Landry, M.R., and Cassar, N.: Lagrangian studies of marine production: A multimethod assessment of productivity relationships in the California Current Ecosystem upwelling region. Journal of Geophysical Research: Oceans, 125, e2019JC015984. doi:10.1029/2019JC015984, 2020.

Krause, M.: Vertical distributions of fecal pellets during FLEX '76. Helgolander Meersesunters, 34(3), 313-327, doi:10.1007/BF02074125, 1981.

Kwon, E. Y., Primeau, F., and Sarmiento, J. L.: The impact of remineralization depth on the air–sea carbon balance. Nature Geoscience, 2, 630. doi:10.1038/ngeo612, 2009.

Lam, P.J., Bishop, J.K.B., Henning, C. C., Marcus, M.A., Waychunas, G. A. and Fung, I.Y.: Wintertime phytoplankton bloom in the Subarctic Pacific supported by Continental Shelf Iron., Global Biogeochemical Cycles. 20, 12pp. GB1006, doi:10.1029/2005GB002557, 2006.

Lam, P. J., and Bishop, J. K. B.: High biomass, low export regimes in the Southern Ocean. Deep-Sea Research Part II: Topical Studies in Oceanography, 54(5–7), 601–638, doi:10.1016/j.dsr2.2007.01.013, 2007.

Lerman A., D. Lal and M. F. Dacey (1975) Stokes' settling and chemical reactivity of suspended particles in natural waters. In: Suspended solids in water. R. J. GIBBS, editor, Plenum Press, pp. 17 47.

Li, Z., and Cassar, N., Satellite estimates of net community production based on O2/Ar observations and comparisons to other estimates, Global Biogeochemical Cycles, 30, 735–752, doi: 10.1002/2015GB005314, 2016.

Lutz, M., Caldeira, K., Dunbar, R., and Behrenfeld, M.: Seasonal rhythms of net primary production and particulate organic carbon flux to depth describe the efficiency of biological pump in the global ocean, J. Geophys. Res.-Oceans, 112, C10011, doi:10.1029/2006JC003706, 2007.

Lynn, R. J. and Simpson, J. J.: The California Current System: The Seasonal Variability of its Physical Characteristics, Journal of Geophysical Research: Oceans, 92 (12), 12947–12966, doi:10.1029/JC092iC12p12947, 1987.

Madin, L.P., and Purcell, J.E.: Feeding, metabolism and growth of Cyclosapa Bakeri in the subarctic Pacific, Limnology and Oceanography, 37(6), 1236-1251, doi:10.4319/lo.1992.37.6.1236, 1992.

Marsay, C. M., Sanders, R. J., Henson, S., Pabortsava, K., and Achterberg, E.P.,: Attenuation of sinking particulate organic carbon flux through the mesopelagic ocean. Proceedings of the National Academy of Sciences, 112 (4) 1089–1094, doi:10.1073/pnas.1415311112, 2015.

Martin, J.H., Knauer, G.A., Karl, D.M., and Broenkow, W.W.: VERTEX: carbon cycling in the northeast Pacific. Deep Sea Research Part A. Oceanographic Research Papers, 34(2), 267–285. doi:10.1016/0198-0149(87)90086-0, 1987.

McPhee-Shaw, E.E., Sternberg, R.W., Mullenbach, B. and Ogston, A.S.: Observations of intermediate nepheloid layers on the northern California continental margin, Continental Shelf Research, 24(6), 693-720, doi:10.1016/j.csr.2004.01.004, 2004.

Ohman, M., Barbeau, K., Franks, P., Goericke, R., Landry, M., and Miller, A.: Ecological Transitions in a Coastal Upwelling Ecosystem. Oceanography, 26(3), 210–219. doi:10.5670/oceanog.2013.65, 2013.

Omand, M. M., Asaro, E.A., Lee, C.M., Perry, M.J., Briggs, N., Cetinić, I., and Mahadevan, A.: Eddy-driven subduction exports particulate organic carbon from the spring bloom, Science, 348, 222-225. doi: 10.1126/science.1260062, 2015.

Pak, H., Zaneveld, R. V. and Kitchen J.: Intermediate Nepheloid Layers Observed off Oregon and Washington. Journal of Geophysical Research: Oceans, 85(11), 6697-6708, doi.org/10.1029/JC085iC11p06697, 1980.

Passow, U., and Carlson, C.A.: The biological pump in a high CO2 world. Marine Ecology Progress Series, 470, 249–271. doi:10.3354/meps09985, 2012.

1055 Pomeroy, L.R., Hanson, R.B., McGillivary, P.A., B.F. Sherr, D. Kirchman, D., and Deibel, D.: Microbiology and chemistry of fecal products of pelagic turnicates: rates and fates. Bull. Mar. Sci., 35 (3), 426–439, 1984.

Saba, G. K., and Steinberg, D. K.: Abundance, composition, and sinking rates of fish fecal pellets in the santa barbara channel. Scientific Reports, 2, 1–6. doi:10.1038/srep00716, 2012.

Sasaki, H., Hattori, H., and Nishizawa, S.,: Downward flux of particulate organic matter and vertical distribution of calanoid 1060 copepods in the Oyasio Waters in the summer. Deep-Sea Research Part A, 35, 505–515. doi:10.1016/0198-0149(88)90128-8, 1988.

Sato, R., Tanaka, Y., and Ishimaru, T.: House Production by Oikopleura dioica (Tunicata, Appendicularia) Under Laboratory Conditions. Journal of Plankton Research, 23(4), Pages 415–423, https://doi.org/10.1093/plankt/23.4.415. 2001.

Schneider, N., Lorenzo, E.D., and Niler, P. P.: Salinity Variations in the Southern California Current. J. Phys. Ocean. 35, 1065 1421–1436. doi:10.1175/JPO2759.1, 2005.

Siegel, D. A., Buesseler, K. O., Doney, S. C., Sailley, S. F., Behrenfeld, M. J., and Boyd, P. W.: Global assessment of ocean carbon export by combining satellite observations and food-web models. Global Biogeochemical Cycles, 28, 181–196. doi:10.1002/2013GB004743, 2014.

Siegel, D. A., Buesseler, K. O., Behrenfeld, M. J., Benitez-nelson, C. R., Boss, E., Brzezinski, M. A., Burd, A., Carlson, C. 1070 A., D'Asaro, E. A., Doney, S. C., Perry, M. J., Stanley, R. H. R., and Steinberg, D. K.: Prediction of the Export and Fate of Global Ocean Net Primary Production : The EXPORTS Science Plan, 3(March), 1–10. doi:10.3389/fmars.2016.00022, 2016.

Siegelman-Charbit, L., Koslow, J. A., Jacox, M. G., Hazen, E. L., Bograd, S. J., and Miller, E. F.: Physical forcing on fish abundance in the southern California Current System. Fisheries Oceanography, 27, 475–488. doi:10.1111/fog.12267, 2018.

Silver, M. W., Coale, S. L., Pilskaln, C. H., and Steinberg, D. R.: Giant aggregates: Importance as microbial centers and agents 1075 of material flux in the mesopelagic zone. Limnology and Oceanography, 43(3), 498–507. doi:10.4319/lo.1998.43.3.0498, 1998.

Smetacek, V.S.: Zooplankton standing stock, copepod faecal pellets and particulate detritus in Kiel bight, Estuarine and Coastal Marine Science, 11, 477–490, doi: 10.1016/S0302-3524(80)80001-6, 1980.

Stanley, R. H. R., Doney, S. C., Jenkins, W. J., and Lott, D. E.: Apparent oxygen utilization rates calculated from tritium and helium-3 profiles at the Bermuda Atlantic Time-series Study site. Biogeosciences, 9(6), 1969–1983. doi:10.5194/bg-9-1969-2012, 2012.

Stemmann, L., Prieur, L., Legendre, L., Taupier-Letage, I., Picheral, M., Guidi, L. and Gorsky, G.: Effects of frontal processes on marine aggregate dynamics and fluxes: an interannual study in a permanent geostrophic front (NW Mediterranean), Journal of Marine Systems, 70, 1–20. doi:10.1016/j.jmarsys.2007.02.014, 2008.

Steinberg, D. K., Van Mooy, B.A.S., Buesseler, K.O., Boyd, P.W., Kobari, T. and Karl, D.M.: Bacterial vs. zooplankton control of sinking particle flux in the ocean's twilight zone. Limnology and Oceanography. 53(4): 1327–1338. doi:10.4319/lo.2008.53.4.1327, 2008.

Stukel, M. R., Ohman, M. D., Benitez-Nelson, C. R., and Landry, M. R.: Contributions of mesozooplankton to vertical carbon export in a coastal upwelling system. Marine Ecology Progress Series, 491, 47–65. doi:10.3354/meps10453, 2013.

Stukel, M. R., Asher, E., Couto, N., Schofield, O., Strebel, S., Tortell, P., and Ducklow, H. W.: The imbalance of new and export production in the western Antarctic Peninsula, a potentially "leaky" ecosystem. Global Biogeochemical Cycles, 29, 1400–1420. doi:10.1002/2015GB005211, 2015.

Stukel, M. R., Song, H., Goericke, R., and Miller, A. J.: The role of subduction and gravitational sinking in particle export , carbon sequestration , and the remineralization length scale in the California Current Ecosystem, Limnology and Oceanography, 63, 363–383. doi:10.1002/lno.10636, 2018.

Stukel, M. and Landry, M.: California Current Ecosystem LTER: Exported particulate carbon and nitrogen measurements from 4-day sediment trap deployments in the CCE region, 2007 - 2017 (ongoing). ver 6. Environmental Data Initiative. https://doi.org/10.6073/pasta/de679918c44266dcebbc5f85a37dcd36. 2020.

Turner, J.T.: Progress in Oceanography Zooplankton fecal pellets , marine snow , phytodetritus and the ocean ' s biological pump. Progress in Oceanography, 130, 205–248. doi:10.1016/j.pocean.2014.08.005, 2015.

Whitmore, B. M., Nickels, C. F. and Ohman, M. D.: A comparison between Zooglider and shipboard net and acoustic mesozooplankton sensing systems. Journal of Plankton Research 41, 521-533 doi:10.1093/plankt/fbz033, 2019.

Wong, C.S., Whitney, F.A. , Crawford, D.W., Iseki, K., Matear, R.J., Johnson, W.K., Page, J.S., and Timothy, D. Seasonal and interannual variability in particle fluxes of carbon, nitrogen and silicon from time series of sediment traps at Ocean Station P, 1982 - ì1993: relationship to changes in subarctic primary productivity, Deep Sea Research Part II: Topical Studies in Oceanography, 46 (11-12), 2735-2760, 1999. https://doi.org/10.1016/S0967-0645(99)00082-X

Yao, X., and Schlitzer, R.: Assimilating water column and satellite data for marine export production estimation. Geoscientific Model Development, 6(5), 1575–1590. doi:10.5194/gmd-6-1575-2013, 2013.

1110   Data Availability.

All data sources are described in the Methods section.

Table 1. Carbon Flux Explorer deployments during CCE-LTER process study P1706 June 2 – July 1, 2017.

Cycle[1]	Location[2]	CFE Name	Deploy UTC date[3]	Deploy Day[4]	Deploy Latitude	Deploy Longitude	Recovery Day[4]	Recovery Latitude	Recovery Longitude
1	L1	CFE-2-Cal	20170609	159.9917	35.0739	-121.1281	160.8694	35.0187	-121.1653
1	L1	CFE-1	20170610	161.1215	35.0000	-121.1686	162.4806	34.9088	-121.2132
1	L1	CFE-3	20170610	161.0818	35.0000	-121.1686	162.4701	34.9047	-121.1995
1	L1	CFE-2-Cal	20170611	161.9999	34.9396	-121.2031	162.5528	34.9204	-121.2256
1	L1	CFE-4-Cal	20170611	162.0197	34.9348	-121.1946	162.5819	34.9061	-121.2074
2	L2a	CFE-1	20170613	164.1597	34.7391	-121.8349	167.4826	34.9788	-122.4062
2	L2a	CFE-3	20170613	164.1782	34.7391	-121.8349	167.4972	34.9613	-122.4558
2	L2a	CFE-2-Cal	20170614	164.9700	34.7771	-122.0572	166.0451	34.8913	-122.3356
2	L2a	CFE-4-Cal	20170614	164.9822	34.7742	-122.0587	165.9201	34.8850	-122.3084
2	L2b	CFE-2-Cal	20170616	166.5817	34.7098	-122.3004	167.5375	34.7051	-122.4151
2	L2b	CFE-4-Cal	20170616	166.5952	34.7091	-122.2998	167.5500	34.7082	-122.4188
3	L3	CFE-1	20170619	169.9880	34.2382	-123.1001	170.8958	34.1973	-123.0502
3	L3	CFE-2-Cal	20170619	170.1173	34.2275	-123.1480	170.9007	34.1716	-123.0759
3	L3	CFE-1	20170621	171.1496	34.1129	-122.9885	172.5139	34.0782	-122.8477
3	L3	CFE-2-Cal	20170621	171.1150	34.1137	-122.9939	171.9257	34.0773	-122.8891
3	L3	CFE-4-Cal	20170621	171.1310	34.1086	-122.9823	171.9243	34.0734	-122.8689
4	L4	CFE-1	20170623	174.1295	34.4032	-123.0964	176.5160	34.4452	-123.0978
4	L4	CFE-2-Cal	20170623	174.2182	34.4070	-123.0958	174.9417	34.4240	-123.0342
4	L4	CFE-4-Cal	20170623	174.1028	34.4024	-123.1040	174.9174	34.4294	-123.0595
4	L4	CFE-2-Cal	20170625	175.0991	34.4218	-123.0168	176.5340	34.4521	-123.0161
4	L4	CFE-4-Cal	20170625	175.1102	34.4221	-123.0133	176.5132	34.4835	-122.9888

1. CCE-LTER Cycle number; 2. Location Number used in this paper; 3. Deploy Date (YYYYMMDD); 4. Day – year days since Jan 1, 2017 0000 UTC. Jan 1, 2017 at 1200 UTC= 0.5.

115

Table 2. Hydrographic and Euphotic Zone Properties at CCE-LTER P1706 study locations

Location	Mean MLD$_{24}$ (m)	MLD range (m)	Z$_{eu}$ (SAT) (m)	Z$_{eu}$ (PAR) (m)	Z$_{eu}$ (PAR) range (m)	Mean 0–20 m NO$_3$ (μM)	σ$_θ$ @ euphotic base (kg m^{-3})	Mean 0-20 m Salinity (PSU)	Mean 0-20 m c$_p$ (m^{-1})	Stock 0–45 m POC (mmol m^{-2})	Stock 0–45 m NO$_3$ (mmol m^{-2})
1	19	13–25	21	19	16±4	7.76	25.5	33.748	0.943	685.8	625±59
2a	26	18–36	29	25	25±3	8.02	25.5	33.637	0.763	557.5	616±19
2b	26	18–36	29	25	25±3	7.82	25.5	33.636	0.454	410.2	522±26
4	9	5–14	–	51	51±6	3.15	25.0	33.595	0.159	111.1	371±18
3	27	11–69	77	49	49±7	1.89	25.8	33.160	0.088	103.9	124±18

MLD$_{24}$: daily average mixed layer depth based on σ$_θ$ difference = 0.05 kg m^{-3}; Zeu: euphotic zone depth based on satellite (SAT) or CTD photosynthetically active radiation (PAR) 1% light level.

120

Table 3. Martin Curve Fits to Attenuance Flux (All Dives)

Location	Zref	size bin	Martin Curve 'b'	b-Error	Intercept	intercept Error	SE_y	R^2	n	p
1	50	**30-100**	-1.57	0.51	-0.280	0.297	0.263	0.735	13	**0.0002**
1	50	100-200	-0.97	0.38	-0.175	0.224	0.199	0.648	13	**0.0009**
1	50	**200-400**	-0.24	0.37	0.201	0.216	0.191	0.106	13	0.2771
1	50	**400-1000**	-0.23	0.54	0.081	0.317	0.281	0.048	13	0.4728
1	50	**>1000**	0.62	0.66	0.974	0.386	0.342	0.204	13	0.1214
1	50	**Total**	0.37	0.59	1.176	0.344	0.305	0.105	13	0.2791
2	100	**30-100**	-0.58	0.19	-1.020	0.074	0.130	0.505	29	**<0.0001**
2	100	100-200	-0.80	0.26	-0.455	0.101	0.177	0.510	29	**<0.0001**
2	100	**200-400**	-1.98	0.41	0.871	0.162	0.283	0.717	29	**<0.0001**
2	100	**400-1000**	0.80	0.34	-0.330	0.134	0.234	0.373	29	**0.0004**
2	100	**>1000**	1.57	0.58	0.444	0.232	0.395	0.452	28	**<0.0001**
2	100	**Total**	0.85	0.31	0.925	0.122	0.214	0.451	28	**0.0001**
3	100	**30-100**	-1.61	0.59	-1.026	0.206	0.245	0.657	14	**0.0004**
3	100	**100-200**	-1.57	0.59	-0.586	0.205	0.244	0.646	14	**0.0005**
3	100	200-400	-1.10	0.58	-0.277	0.200	0.238	0.485	14	**0.0056**
3	100	**400-1000**	0.05	0.83	-0.755	0.286	0.341	0.001	14	0.9198
3	100	>1000	-0.44	0.85	0.486	0.304	0.347	0.071	13	0.3797
3	100	Total	-0.45	0.70	0.583	0.242	0.288	0.099	14	0.1653
4	100	30-100	-0.97	0.42	-0.833	0.145	0.229	0.492	19	**0.0008**
4	100	100-200	-0.75	0.50	-0.573	0.174	0.276	0.283	19	**0.0190**
4	100	200-400	-0.66	0.54	-0.225	0.187	0.296	0.213	19	**0.0466**
4	100	400-1000	-0.42	0.66	0.172	0.230	0.364	0.068	19	0.2827
4	100	>1000	-0.21	0.71	1.307	0.246	0.390	0.015	19	0.6180
4	100	Total	-0.24	0.68	1.376	0.238	0.377	0.021	19	0.5538

Notes: b and intercept errors are 95% confidence intervals p denotes the probability that slope is zero. **Bold**: <0.05

Table 4. Martin Curve parameters for PIT trap data (Z_{ref} = euphotic depth)

Location	data fit	Martin 'b'	b-Error	Intercept	intercept Error	SE (y)	R^2	n	p
L1	pit	**-0.367**	**0.268**	1.582	0.200	0.117	0.406	11	**0.0349**
L1	pit+np	-0.783	0.337	1.908	0.240	0.195	0.636	12	**0.0019**
L2	pit	-0.864	0.222	1.796	0.131	0.089	0.847	11	**< 0.0001**
L2	pit+np	-1.113	0.258	1.954	0.146	0.129	0.857	12	**< 0.0001**
L2toL4	pit	-0.989	0.189	1.621	0.061	0.057	0.965	6	**0.0005**
L2toL4	pit+np*	-1.192	0.572	1.723	0.172	0.187	0.766	7	**0.0099**
L3	pit	**-2.013**	**0.508**	1.786	0.172	0.133	0.886	9	**0.0002**
L3	pit+np	**-2.024**	**0.406**	1.790	0.130	0.125	0.913	10	**< 0.0001**
L4	pit	**-0.301**	**0.185**	1.537	0.062	0.063	0.526	10	**0.0175**
L4	pit+np	**-0.163**	**0.258**	1.480	0.083	0.097	0.127	11	**0.0066**

Notes: errors are 95% confidence intervals. **Bold**: $p < 0.05$ or b significantly different from Martin b = -0.86. p denotes the probability that slope is zero; *New Production based POC export is estimated NO_3 inventory change between L2 and L4.

Table 5. Martin Curve Fits to Number Flux (All Dives)

Location	Zref	size bin	Martin Curve 'b'	b-Error	Intercept	intercept Error	SE_y	R2	n	p
1	50	**30-100**	**-1.57**	0.47	6.486	0.278	0.247	0.759	13	**0.0001**
1	50	100-200	-1.26	0.42	5.632	0.245	0.217	0.723	13	**0.0002**
1	50	200-400	-0.73	0.38	5.099	0.224	0.199	0.511	13	**0.0060**
1	50	400-1000	-0.85	0.43	4.386	0.252	0.224	0.531	13	**0.0047**
1	50	**>1000**	**0.14**	0.45	3.834	0.267	0.236	0.028	13	0.5826
1	50	**Total**	**-1.43**	0.44	6.560	0.261	0.231	0.750	13	**0.0001**
2	100	**30-100**	**-0.55**	0.18	5.761	0.072	0.125	0.494	29	**<0.0001**
2	100	**100-200**	**-0.53**	0.24	5.068	0.096	0.168	0.341	29	**0.0009**
2	100	**200-400**	**-1.69**	0.41	5.440	0.162	0.283	0.646	29	**<0.0001**
2	100	**400-1000**	**0.31**	0.30	3.833	0.120	0.211	0.102	29	0.0907
2	100	**>1000**	**1.26**	0.46	3.414	0.183	0.312	0.462	28	**<0.0001**
2	100	Total	-0.67	0.17	5.993	0.066	0.115	0.638	28	**<0.0001**
3	100	**30-100**	**-1.30**	0.47	5.537	0.162	0.193	0.669	14	**0.0003**
3	100	**100-200**	**-2.17**	0.71	5.269	0.247	0.293	0.708	14	**0.0002**
3	100	200-400	-1.32	0.53	4.441	0.184	0.219	0.618	14	**0.0009**
3	100	400-1000	-0.49	0.61	3.480	0.212	0.252	0.144	14	0.1802
3	100	>1000	-0.31	0.60	3.235	0.215	0.245	0.071	13	0.3799
3	100	**Total**	**-1.47**	0.51	5.748	0.177	0.211	0.683	13	**0.0004**
4	100	30-100	-0.91	0.42	5.915	0.145	0.230	0.459	19	**0.0014**
4	100	100-200	-0.78	0.53	5.190	0.183	0.291	0.277	19	**0.0206**
4	100	200-400	-0.69	0.60	4.698	0.209	0.332	0.188	19	0.0638
4	100	400-1000	-0.45	0.71	4.189	0.248	0.394	0.064	19	0.2946
4	100	>1000	-0.29	0.56	4.018	0.195	0.309	0.045	19	0.3829
4	100	Total	-0.86	0.45	6.024	0.155	0.246	0.395	19	**0.0004**

Notes: b and intercept errors are 95% confidence intervals. p denotes the probability that slope is zero. **Bold**: <0.05

140
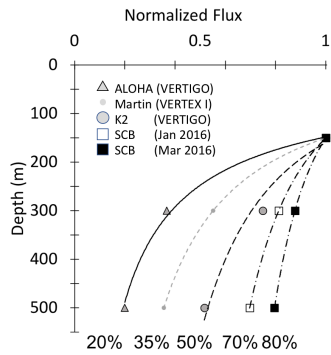
Figures.

Figure 1. Martin curves normalized to 150 m. Representative data from Martin et al. (1987), Buesseler et al., (2007) and Bishop et al., (2016). "b" values of lines from left to right are: -1.33 (Stn. ALOHA), -0.86 (VERTEX I), -0.51 (Stn. K2), -0.19 and -0.3 (March and Jan 2016, Santa Cruz Basin). Transport efficiencies between 150 and 500 m range from 20% (ALOHA) to 80% (Santa Cruz Basin).
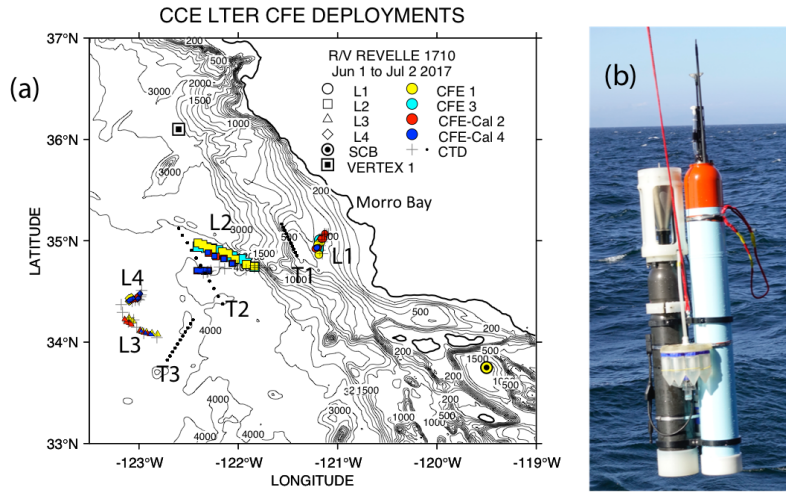
Figure 2. (a) CFE and CTD deployments at locations L1 to L4. The CTD stations were close to a drifting surface drogued productivity array. For the majority of stations, the CTDs and CFEs were close to one another. However, at L2, the CFEs diverged to the west-north-west of the drogued drifters. Dots depict locations of cross-filament CTD particle–optics transects T1, T2, and T3. T1 preceded work at L1; T2 was occupied after completion of sampling at L2. T3 was completed after work at L4. Data from transects shown in Fig. 11. (b) CFE-Cal during recovery.
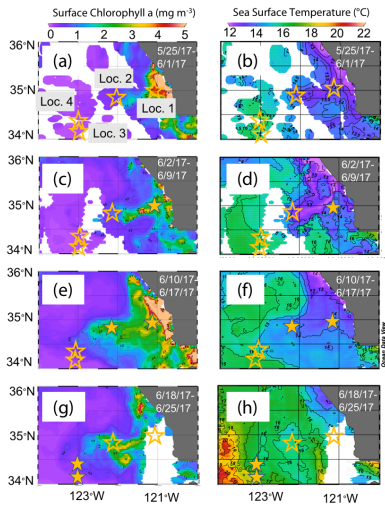
Figure 3. Remotely sensed surface chlorophyll (a,c,e,g) and sea surface temperature (SST) (b,d,f,h) maps of the study area from late May to the end of June 2017. All images are from 4 km resolution, 8-day averaged data from NASA Ocean Colour from SNPP VIIRS. The stars represent locations 1 to 4 where CFEs were deployed. Stars are filled in in the panels most closely corresponding to the time of observations.
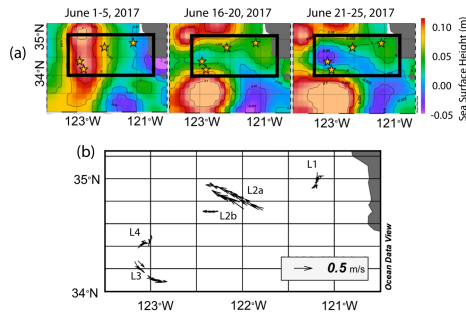
Figure 4. (a) Average sea surface height from June 1-5, 16-20 and 21-25 2017. In the beginning of June, sea surface height was low near the shore due to Ekman transport, and higher off the coast. As the filament developed and moved to the west, a sea surface trough formed extending 200 km offshore and was first apparent in the June 16-20 map; it deepens in the June 21-25 map, indicating the formation of a cyclonic eddy; Anti-cyclonic eddies are present to the north and south. Stars represent positions of each location. (b) Velocity vectors for all CFE dives to depths of 500 m. The CFE motions were fastest at locations L2 and L3, where the CFEs were deployed near the edges of the cyclonic eddies and slowest at L1 inshore and at L4 which was located near the centre of the cyclonic eddy.
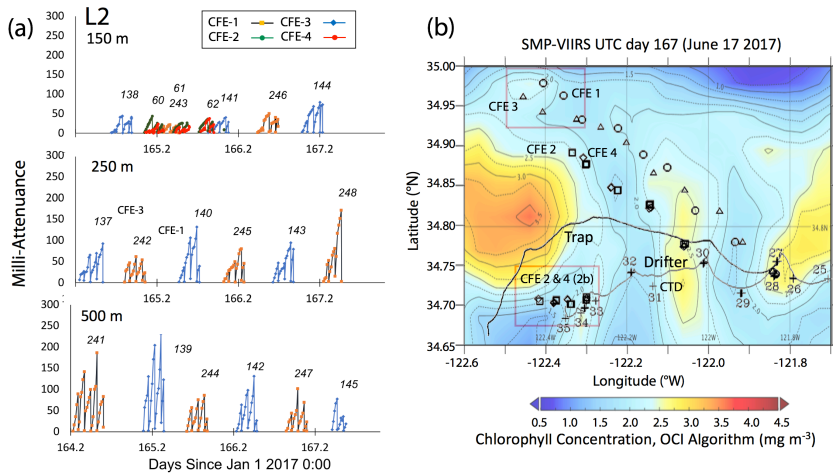
Figure 5. (a). Raw attenuance time series for all CFEs deployed at L2. See Fig. 2 for deployment context. Italicized numbers are the dive numbers corresponding to the data. The mATN timeseries scales with flux as timing is constant. (b). Map showing deployment and trajectories of CFEs, CTD station locations, and tracks of the productivity drifter and sediment trap array during the intensive studies at L2. CFEs 1–4 are indicated by circle, square, triangle, and diamond symbols, respectively. The overlay is the SMPP-VIIRS chlorophyll field for June 17, 2017– during the later stages of sampling at this location.
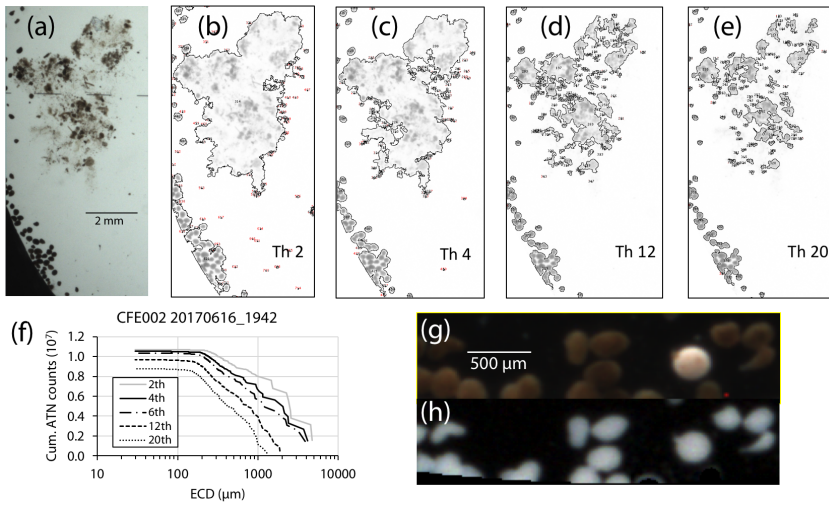
Figure 6. Top: (a) Segment of a CFE-2 transmitted light image June 2017 at 1942 UTC; depth 150 m. Panels (b – e): ImageJ particle outline maps at attenuance thresholds of 0.02, 0.04, 0.12, and 0.20, superimposed on the attenuance image for the sample. Darker greys denote higher attenuance. We found that touching faecal pellets could not be separated even at a threshold of 0.20 ATN. At thresholds >0.06, large low-density aggregates are seen as highly fragmented and the contribution of smaller particles is reduced. Lower: (f) Particle size attenuance count distributions as a function of threshold. (g) Magnified image under dark field illumination. Olive coloured faecal pellets are readily distinguished from an unidentified egg. (h) Attenuance map of the same view.
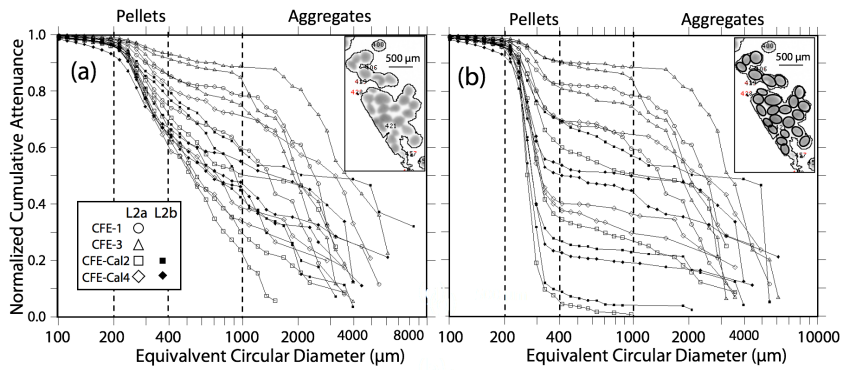
Figure 7. Processed size distribution data for CFEs 1, 2, 3 and 4 deployed near 150 m at L2. Normalized Cumulative Attenuance Flux is plotted against Equivalent Circular Diameter (in μm). (a) original cumulative attenuance size-distributions from ImageJ and (b) after secondary processing to correct for touching particles (see insets in upper rhs corners of (a) and (b)). Boundaries for reduced size categories are 30–100 μm (not shown), 100–200 μm, 200–400 μm, 400–1000 μm, and >1000 μm are indicated in (a and b). Open and closed symbols denote data from the first and second deployments of the CFE-Cals at location 2 designated as L2a and L2b, respectively. After correction, the 400-1000 μm size category contributed little to sample attenuance.
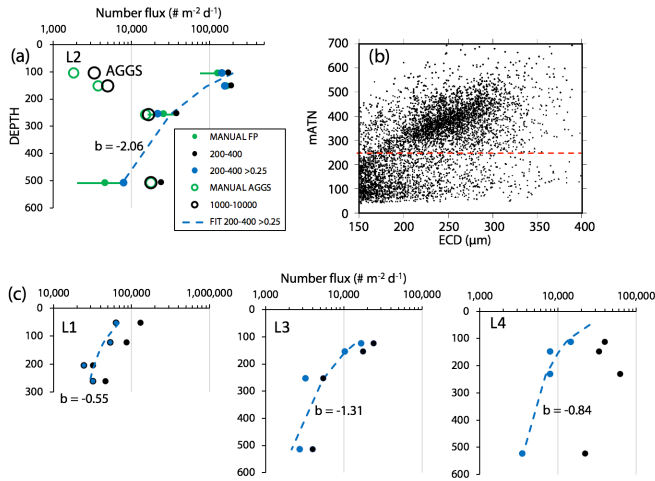
Figure 8. (a) Profile of aggregate and pellet number fluxes determined by Method 3 and by manual counting at Location L2. The small blue filled circles represent number flux of 200–400 μm particles with average attenuance >0.25. These data agree closely with manually enumerated pellet counts. Method 3 counted more aggregates in the shallowest samples because the manual method was unable to infer weakly defined boundaries of less dense aggregates. Data are tabulated in Appendix A, Table 1.1. (b) Plot of average particle attenuance vs. equivalent circular diameter (ECD). The red dashed line denotes the lower boundary of the cluster of >0.25 ATN particles. (c). Profiles of 200–400 μm total particle number fluxes and for >0.25 ATN particles at L1, L3, and L4. Dashed lines are Martin fits to the ovoid pellet class fluxes. In all cases, fluxes of faecal pellets decrease with depth.
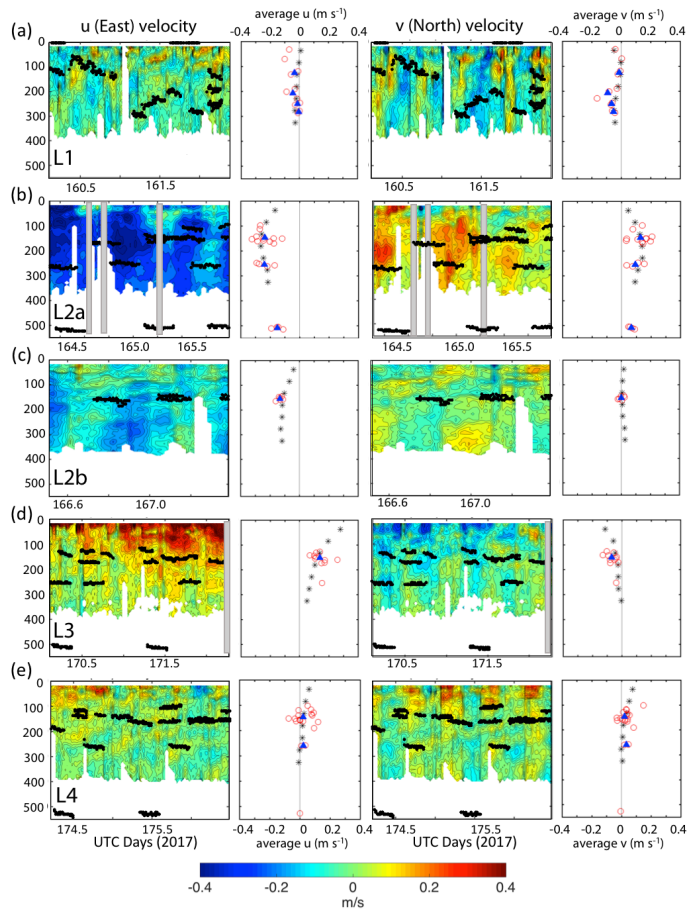
Figure 9. Thirty-second averaged current velocities in u (East positive) and v (North positive) directions from 150 kHz narrow band ADCP data. CFE depths during flux measurements are shown. Profiles denoted by black asterisks to right of each contour plot are averaged ADCP velocities for the entire time span. Red points represent average CFE velocities over the course of each dive. Shaded boxes denote missing data. Filled blue triangles are the averaged CFE velocities for all dives at a given depth. Panels (a), (b), (c), (d), and (e) Locations 1, 2a, 2b, 3 and 4 respectively.

I155
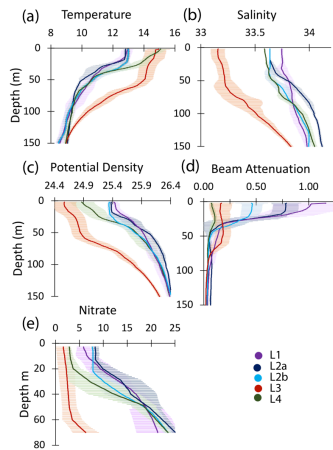
Figure 10. Profiles of averaged T, S, potential density, beam attenuation coefficient (650nm), and nitrate in the upper 150 m at locations L1, L2a, L2b, L3, and L4. Error bars are ± 1 S.D.
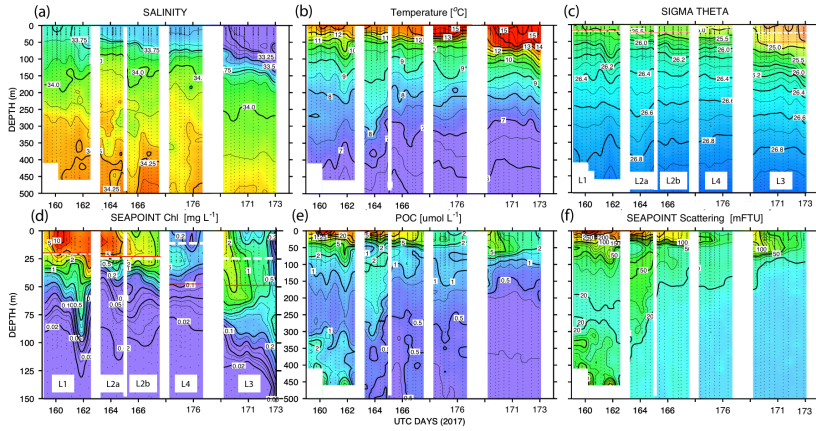
Figure 11. (a) Salinity, (b) temperature, (c) sigma theta (σ_θ), (d) chlorophyll fluorescence, (e) transmissometer derived POC, and (f) turbidity timeseries from CTD casts. The time axis (in UTC days since Jan 1 0000h 2017) has been reordered so that L1, L2, and L4 are grouped. L3 is shifted to the right side of each panel. The white dashed line and red line (c) and (d) denote averaged 24 h mixed layer depths and euphotic zone depths, respectively. The chlorophyll fluorescence (d) depth axis is 150 m; limit of detection was 0.02 units.
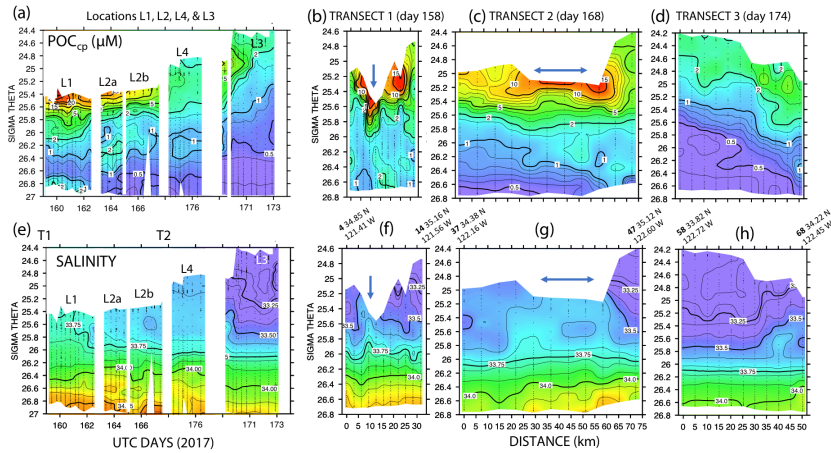
Figure 12. (a) Transmissometer particulate organic carbon (POC) and (e) salinity – potential density time series during the intensive studies at L1, L2a, L2b, L4, and L3. Also shown are cross-filament transects T1, T2, and T3 for POC (b), (c), d) and salinity (f), (g), (h). Transect locations are shown in Fig. 2. Transect T1 (UTC day 158) was located between L1 and L2; T2 (day 168) was sited between L2 and L4; and T3 crossed the outer edge of the filament on day 174 after completion of work at L4. Distances in kilometres. UTC days as defined in Fig. 10. The arrows in (f) and (g) indicate the high salinity surface water in the filament; its scale was ~5 km wide at T1, it was ~25 km wide at T2.

|160
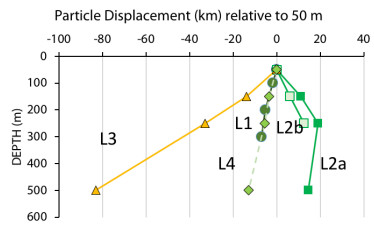
Figure 13. Displacements (in kilometres) in the direction of motion of the filament for particles with a hypothetical sinking rate of 100 m d^{-1} as they sink from 50 m. Extreme displacements were calculated for transitional waters (L3) where sinking particles lagged behind the surface layer by as much as 85 km. Sinking particles would lead the surface layer by 20 km at a depth of 250 m at L2a. Calculated from ADCP velocities in Fig. 9.
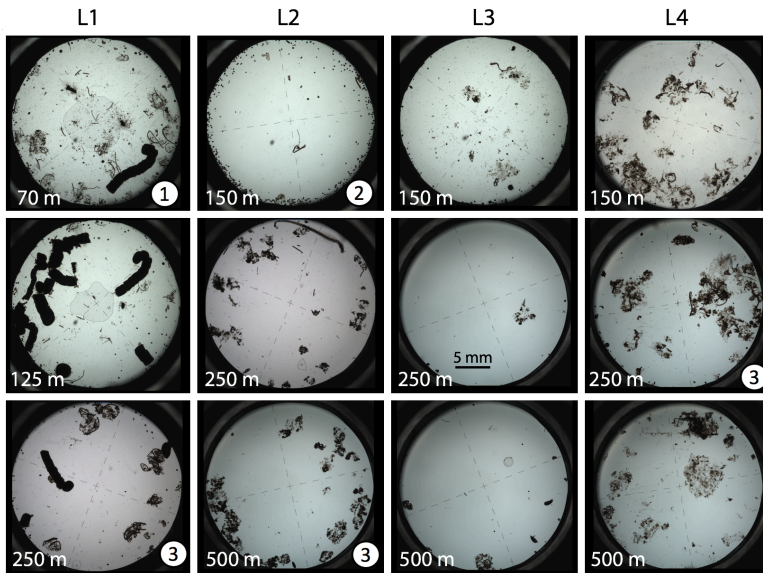
Figure 14. Representative transmitted light imagery of particles sampled by the CFEs at locations L1, L2, L3 and L4. The top row of images is for material captured shallower than ~150 m. Middle row, particles captured near 250 (125 m at L1). Bottom row are images of particles captured near 500 m (250 m at L1). Dashes in the images are 1 mm long. Anchovy faecal pellets are the optically-dense 7–10 mm long particles seen in images at L1 (1). The 150 m sample at L2 is ringed by several hundred ~250 µm sized olive faecal pellets (2). >1000 µm sized Aggregate particles dominate deeper samples at all locations and especially so at L4 (3). A close up of olive-coloured faecal pellets and aggregates is in Figure 6, All imagery is available online.
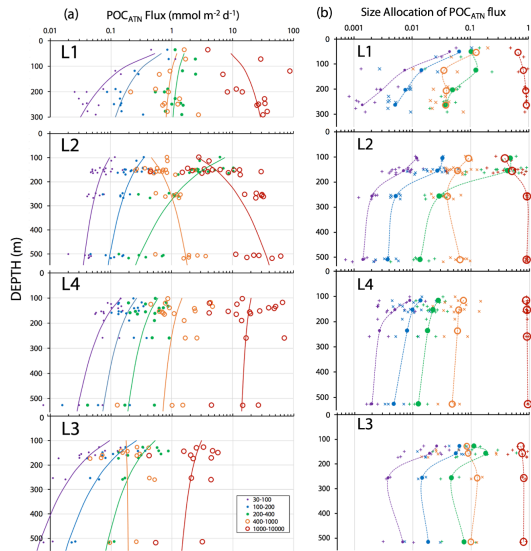
Figure 15. (a) POC_{ATN} flux in mmol C m^{-2} d^{-1} partitioned in 30–100, 100–200, 200–400, 400–1000, and >1000 μm particle size classes for all CFE dives from in-filament locations L1, L2, and L4, and from transitional waters at L3. The curves denote Martin function fits to the data (Table 3). (b) Fraction of POCATN flux allocated to 30-100, 100-200, 200-400, 400-1000, and >1000 μm size fractions. Large symbols connected dashed curves are averages of pooled data, small points correspond to individual dives. Greater than 1000 μm sized aggregates dominated flux in all regimes with the exception of the 100 m at L2.
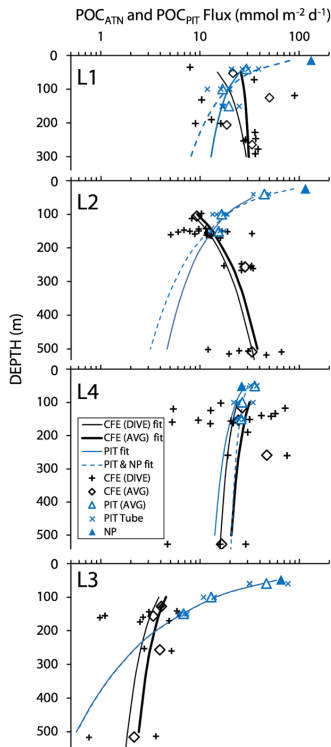
Figure 16. Left: Fraction of POC$_{ATN}$ flux assigned to 30-100, 100-200, 200-400, 400-1000, and >1000 μm size fractions. Dashed lines connect averages of pooled data, small points correspond to individual dives. Greater than1000 μm sized aggregates dominated flux in all regimes with the exception of the 100 m data at L2. Symbol Key is defined in Figure 15. Right: Comparison of CFE, PIT and NP POC flux estimates at the three filament locations L1, L2 and L4 and at L3 in transitional waters. The thin and heavy black lines are the "Martin" curve fit for individual CFE dives (data shown by +) and for pooled time-averaged data (diamonds), respectively. The solid and dashed blue lines denote Martin curves based on fits to PIT (Particle Interceptor Trap) results and to combined PIT result and new production (NP, solid triangle) data. At L1, the blue curves underestimate fluxes 250 m by a factor of 2; At L2 blue curves, underestimate flux by a factor of 6 at 500 m. At L4, there was close agreement among methods. At L3, (with sparse data), fluxes were underestimated by a factor of ~2 at 500 m. POC$_{ATN}$ flux calculated from Volume Attenuance Flux (VAF, mATN cm^2 cm^{-2} d^{-1}), where one VAF unit = 1 mmol C m^{-2} d^{-1} (Bourne et al., 2019). PIT and New Production based carbon flux (mmol C m^{-2} d^{-1}) from Kranz et al. (2020). The larger scatter in individual CFE dive data compared to PIT data is attribute to the fact that results are representative of 5 hours of observations vs. 3-4 days.
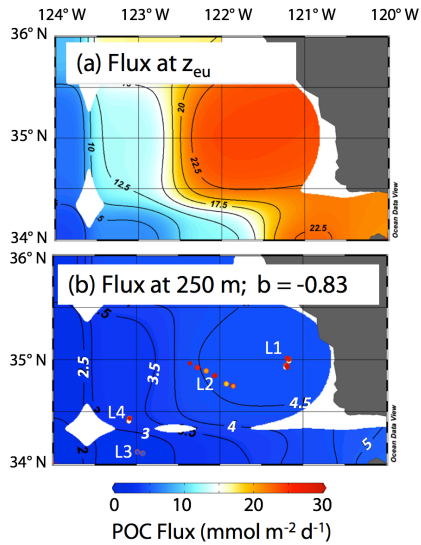
Figure 17. **(a) Euphotic Zone Carbon Export for climatological averaged June from Siegel et al. (2014). (b) fluxes calculated for 250 m using Eqn (1) and the b value from VERTEX I (-0.83; Martin et al., 1987). The euphotic zone depth (z_{eu}) used for the calculation was June climatology from NASA VIIRS. Also shown using the same colour scale are POC_{ATN} flux values near 250 m. The CFE fluxes are far higher than model predictions at depth at all locations except L3.**
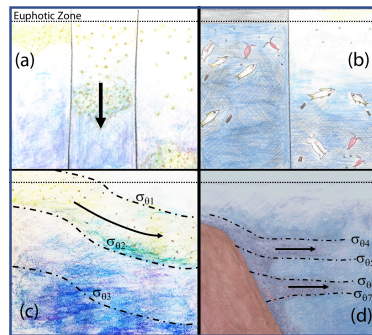
Figure 18. Four mechanisms that can lead to non-classical particle flux profiles. (a) Temporal Delay (Giering et al., 2016); (b) Vertical Migration (Turner, 2015, Bishop et al., 2016); (c) Physical subduction (Omand et al., 2015, Stukel et al., 2018); and (D) Sediment resuspension and lateral advection (Alonso-Gonzalez et al., 2009, Pak et al., 1980, McPhee-Shaw et al., 2004, Chase et al., 2007).
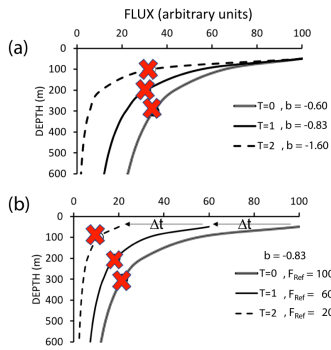
Figure 19. Scenarios which could lead to flux not systematically decreasing with depth. (a) depicts constant flux at the reference depth, with time variant values of the Martin b parameter. (b) depicts a scenario with constant Martin b, but decreasing flux at the reference depth over time (after Giering et al., 2016). Red marks indicate sampling points in both figures, illustrating how temporal delay could lead to observations of increasing flux with depth.
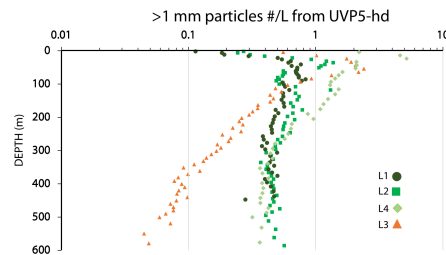
Figure 20. Mean non-living particle number concentrations for >1.024 mm sized aggregates from UVP5-hd profiles. Averages were from pooled CTD casts at filament locations L1, L2, L4, and in transitional waters outside of the filament at L3. Aggregate numbers were more abundant in the waters beneath the filament than in transitional waters below 100m, consistent with CFE observations.

Appendix A.

Table A1-1. Comparison of pellet and aggregate flues from manual enumeration and from particle analysis Method 3.

Depth (m)	Manual Counts							Method 3 results			
	Mean Spherical pellet Flux	Mean Spherical pellet Flux S.D.	Mean Aggregate Flux	Mean Aggregate Flux S.D.	Mean Tubular Pellet Flux	Mean Tubular Flux S.D.	Dives Averaged (n)	>1000 µm Aggregate Flux	200-400 µm Flux	200-400 µm fraction > 0.25 ATN	200-400 µm Flux > 0.25 ATN
105	128415	53895	1832	175	1175	1214	2	3369	179529	0.816	146475
155	169740	25400	3708	926	309	165	15	4943	193440	0.816	157825
258	26043	9854	15023	1680	258	143	5	16403	37830	0.583	22056
509	4671	2654	17680	1956	-44	48	6	17838	24392	0.327	7979

Flux units # m^{-2} d^{-1}. Tubular Pellets > 1000 µm long euphausiid pellets – present without aggregate association.

These data are plotted in Figure 8.

190
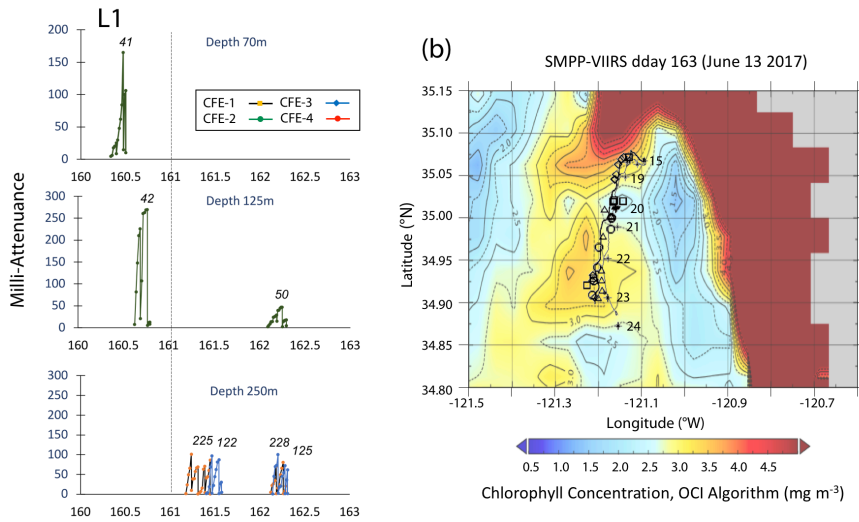
Figure A1-1. (a). Raw attenuance time series for CFEs deployed at L1 (300 m data not shown). See Fig. 2 for deployment context. Italicized numbers are CFE dive numbers. (b). Map showing deployment and trajectories of CFEs, CTD station locations, and tracks of the productivity drifter and sediment trap array during the intensive studies at L1. The overlay is the SMPP-VIIRS chlorophyll field for June 13, 2017. CTD cast numbers are shown on the plot.
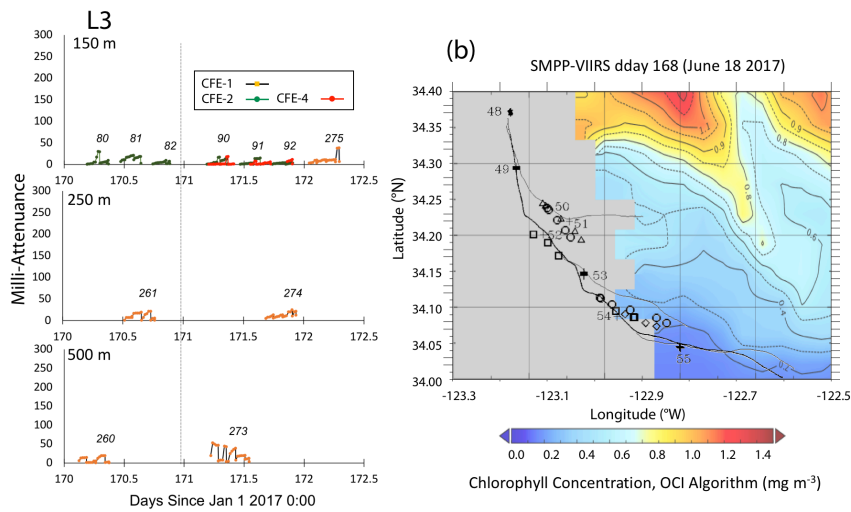
Figure A1-2. (a). Raw attenuance time series for CFEs deployed at L3. See Fig. 2 for deployment context. Italicized numbers are the dive numbers corresponding to the data. (b). Map showing deployment and trajectories of CFEs, CTD station locations, and tracks of the productivity drifter and sediment trap array during the intensive studies at L3. The overlay is the SMPP-VIIRS chlorophyll field for June 18, 2017 – prior to deployments. There is no contemporaneous imagery. CTD cast numbers are shown on the plot.
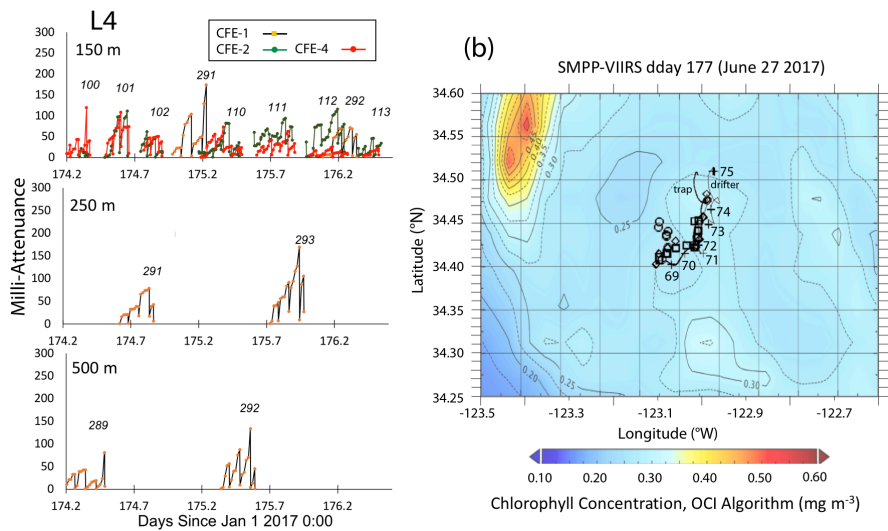
Figure A1-3. (a). Raw attenuance time series for CFEs deployed at L4. See Fig. 2 for deployment context. Italicized numbers are the dive numbers corresponding to the data. (b). Map showing deployment and trajectories of CFEs, CTD station locations, and tracks of the productivity drifter and sediment trap array during the intensive studies at L2. The overlay is the SMPP-VIIRS chlorophyll field for June 27, 2017 – at the end of the period. There is no contemporaneous imagery. CTD cast numbers are shown on the plot.
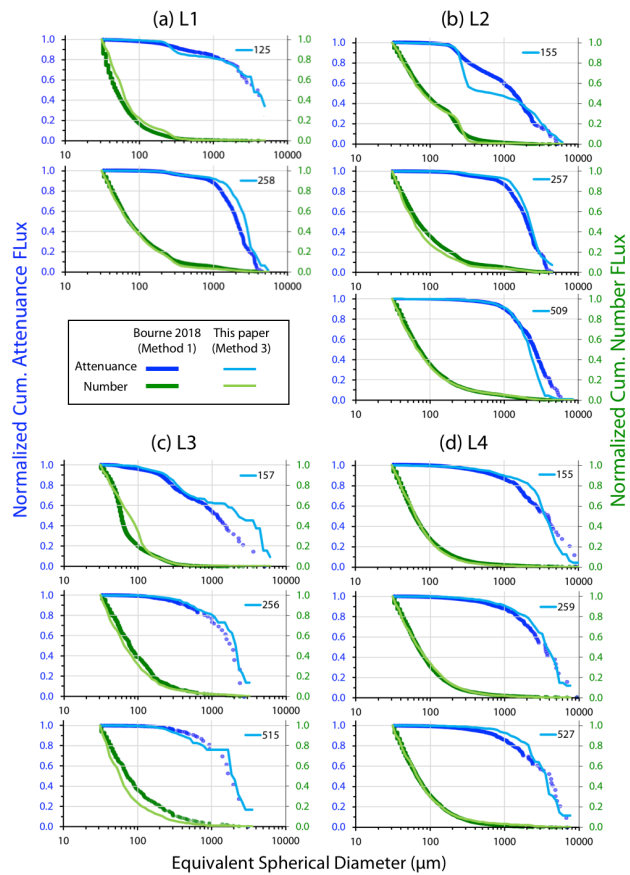
Figure A1-4. Comparison of normalized-cumulative-attenuance flux and normalized-cumulative-number flux size-distributions determined using Methods 1 (Bourne 2018) and 3 (this paper). The darker thicker lines are results from Method 1. In most cases, the two methods compare well at depths of 250 m and 500 m. 150 m data at L2 reflects touching faecal pellets not resolved by Method 1. The 150 m data at L3 show the effects of the Method 1's failure to detect large low attenuance aggregates.
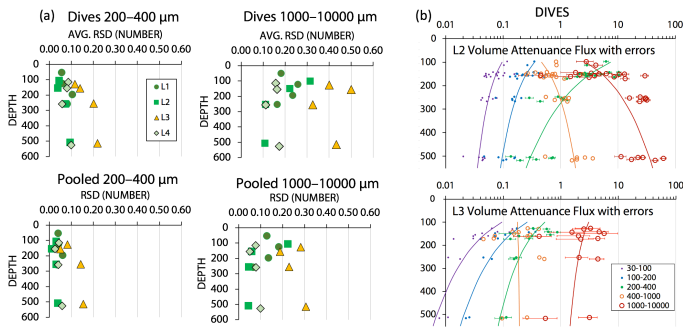
Figure A1-5. (a) Analysis of statistical counting errors for particles in the 200-400 and 1000-10000 μm size categories. The graphs depict averaged relative standard deviations (RSD) for individual dives and for pooled data at 4 depth horizons. (b) We illustrate the contribution of statistical counting error and 9% calibration uncertainty to VAF for the 200-400 and 1000-10000 μm size categories at Loc 2 and Loc 3. In this case there counting errors were based on numbers of particles for each dive. At L2, the contribution of error was a small fraction of the natural variability of >1000 μm VAF results.
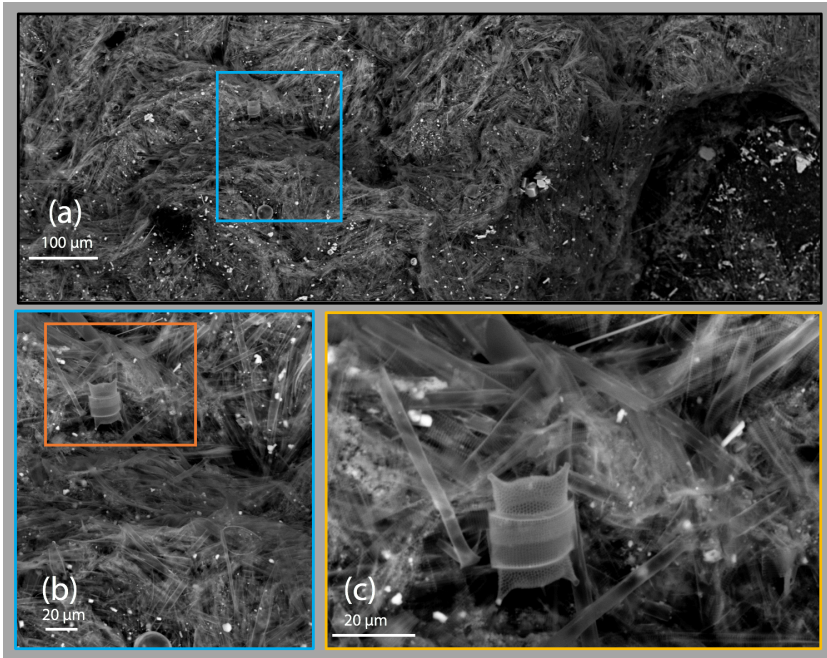
Figure A1-6. Scanning Electron Microscope imagery of an anchovy faecal pellet captured by CFE-Cal at location L1 (see Fig. 14 – L1-125 m). Shown are secondary electron images of the pellet at (a) 244X, (b) 925X, and (c) 2500X magnification. The contents of the pellet are dominated by diatom frustules indicating that anchovies were primary grazers at this location.

CZCS Composite: June 1— 8, Jun 18—25 1984
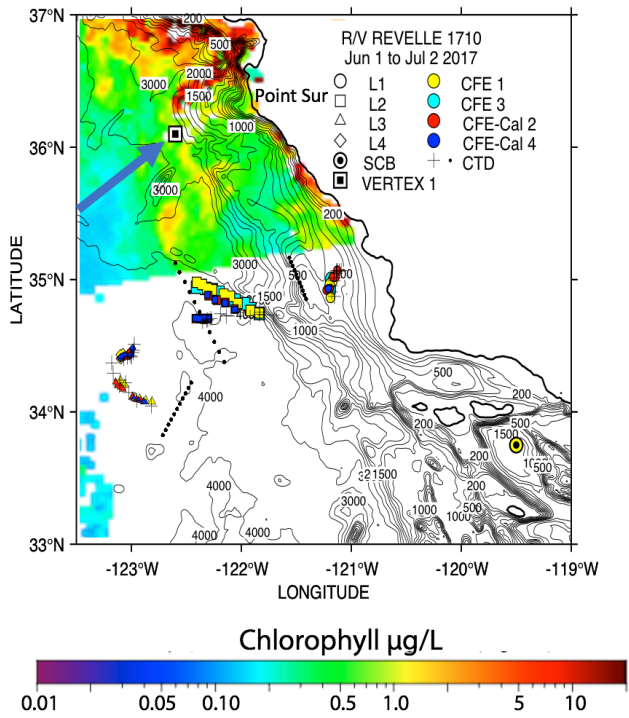
Figure A1-7. June 1984 composite of Coastal Zone Colour Scanner retrievals of surface chlorophyll which shows a chlorophyll-rich filament in the vicinity of the VERTEX 1 location. The imagery is sparse by modern standards.

Don't adjust space between Latin and Asian text, Don't adjust space between Asian text and numbers, Tab stops: 0.39", Left + 0.78", Left + 1.17", Left + 1.56", Left + 1.95", Left + 2.34", Left + 2.73", Left + 3.11", Left + 3.5", Left + 3.89", Le